

Automatic Labeling of Coronary Artery Segments: Multi-Strategy Development and Evaluation

Maren Clapers Colet



Universitat
Pompeu Fabra
Barcelona

Automatic Labeling of Coronary Artery Segments: Multi-Strategy Development and Evaluation

BACHELOR'S THESIS BY

Maren Clapers Colet

UPF Tutor: Pr. Oscar Camara Rey

Supervisor: César Acebes Pinilla

Bachelor's degree in Mathematical Engineering in Data Science

Academic Year 2024 - 2025



Universitat
Pompeu Fabra
Barcelona

Escola
d'Enginyeria



Hospital de
la Santa Creu i
Sant Pau



SANT PAU
Dimension Lab

Acknowledgments

I would like to start by expressing my sincere gratitude to César Acebes Pinilla, my supervisor, for his invaluable guidance throughout this project. Thank you for sharing your knowledge, for helping me develop my research skills, and for introducing me to the field of coronary arteries.

I am also sincerely thankful to Pr. Oscar Camara Rey, my tutor, for his constructive criticism, continuous support, and insightful ideas. Thank you for showing me how engineering can be applied meaningfully in the medical field.

I would also like to thank Dr. Rubén Leta Petracca, cardiologist at Hospital de la Santa Creu i Sant Pau, for generously sharing his medical expertise and for guiding me through the clinical aspects of this work.

Last but not least, I would like to express my heartfelt thanks to my family and friends for their unconditional support throughout this academic year. Thank you for your confidence in me and for standing by my side through the most challenging moments. Your presence and motivation have made all the difference.

Abstract

This bachelor's thesis addresses the automatic labeling of coronary artery segments from 3D binary masks, following standard clinical guidelines. This task is a key step in the diagnosis of coronary artery disease that enables cardiologists to localize the disease, assess its severity, and plan effective treatments. The work was conducted in collaboration with the Hospital de la Santa Creu i Sant Pau, within a broader artificial intelligence-assisted framework aimed at the diagnosis of coronary artery disease. Several strategies were developed and analyzed, including heuristic methods based on anatomical rules, classical machine learning using coordinate and graph features, graph neural networks, and direct multi-class segmentation techniques. The project also involved the creation of a clinically validated labeled dataset. Results highlight the strengths and limitations of each approach, offering insights into their clinical applicability. The study contributes to advancing automation in cardiac diagnosis by developing and evaluating robust coronary segment labeling methods.

Resum

Aquest treball de fi de grau aborda l'etiquetatge automàtic dels segments de les artèries coronàries a partir de màscares binàries 3D, seguint les pautes clíiques estàndard. Aquesta tasca constitueix un pas clau en el diagnòstic de la malaltia coronària que permet als cardiólegs localitzar la malaltia, avaluar-ne la gravetat i planificar tractaments eficaços. El treball s'ha dut a terme en col·laboració amb l'Hospital de la Santa Creu i Sant Pau, dins d'un marc més ampli assistit per intel·ligència artificial dirigit al diagnòstic de la malaltia de les artèries coronàries. S'han desenvolupat i analitzat diverses estratègies, incloent-hi mètodes heurístics basats en regles anatòmiques, models clàssics d'aprenentatge automàtic utilitzant coordenades i característiques de graf, xarxes neuronals gràfiques i tècniques directes de segmentació multiclasse. El projecte també ha inclòs la creació d'un conjunt de dades etiquetat i validat clínicament. Els resultats posen de manifest els punts forts i les limitacions de cada enfocament, oferint una visió sobre la seva aplicabilitat clínica. L'estudi contribueix a l'avenç de l'automatització del diagnòstic cardíac mitjançant el desenvolupament i l'avaluació de mètodes robustos d'etiquetatge coronari.

Resumen

Este trabajo de fin de grado aborda el etiquetado automático de los segmentos de las arterias coronarias a partir de máscaras binarias 3D, siguiendo las guías clínicas estándar. Esta tarea constituye un paso clave en el diagnóstico de la enfermedad arterial coronaria que permite a los cardiólogos localizar la enfermedad, evaluar su gravedad y planificar tratamientos efectivos. El trabajo se ha llevado a cabo en colaboración con el Hospital de la Santa Creu i Sant Pau, dentro de un marco más amplio asistido por inteligencia artificial dirigido al diagnóstico de la enfermedad de las arterias coronarias. Se han desarrollado y analizado diversas estrategias, incluyendo métodos heurísticos basados en reglas anatómicas, modelos clásicos de aprendizaje automático utilizando coordenadas y características de grafo, redes neuronales gráficas y técnicas directas de segmentación multiclase. El proyecto también ha incluido la creación de un conjunto de datos etiquetado y validado clínicamente. Los resultados ponen de relieve los puntos fuertes y las limitaciones de cada enfoque, ofreciendo una visión sobre su aplicabilidad clínica. El estudio contribuye al avance de la automatización del diagnóstico cardíaco mediante el desarrollo y la evaluación de métodos robustos de etiquetado coronario.

Contents

List of figures	xi
List of tables	xi
1 INTRODUCTION	1
1.1 Clinical motivation and context	1
1.1.1 Coronary arteries	1
1.1.2 Coronary artery disease	2
1.1.3 Coronary artery segments	2
1.2 Clinical challenges at Hospital de la Santa Creu i Sant Pau	4
1.2.1 Diagnostic workflow and associated limitations	4
1.2.2 Coronary segment identification	5
1.3 State of the art: overview of existing automatic coronary labeling approaches	6
1.4 Project scope and contributions	7
1.5 Objectives	8
2 METHODOLOGY	9
2.1 Workflow overview	9
2.2 Coronary segments dataset	10
2.2.1 Clinically-guided ground truth creation	10
2.2.2 Centerline extraction	11
2.3 Geometry- and structure-based labeling strategies	13
2.3.1 Curvature and bifurcation method	13
2.3.2 Heuristic and topological rule-based method	13
2.3.3 Final heuristic-based method	16
2.4 Machine learning-based labeling strategies	18
2.4.1 Coordinate-based method	18
2.4.2 Graph features-based method	19
2.4.3 Segment transition detection method	20
2.5 Graph neural network labeling strategy	20
2.6 Direct multi-class segmentation strategy	21
2.7 Evaluation	21
3 RESULTS	23
3.1 Dataset creation	23
3.2 Geometry- and structure-based labeling	25
3.3 Machine learning-based labeling	27

3.4	Graph neural network labeling	30
3.5	Multi-class segmentation labeling	31
4	DISCUSSION	33
4.1	Interpretation of the results	33
4.2	Challenges and limitations	35
4.3	Potential improvements and future lines of research	37
5	CONCLUSION	38
A	CORONARY SEGMENT GUIDELINES	43
A.1	Right coronary artery	43
A.2	Left coronary artery	45
B	EXAMPLE OF MOTION ARTIFACT	49
C	GRAPH-BASED FEATURES	50
D	DEEP LEARNING MODELS TRAINING CURVES	51
D.1	GraphSAGE training curves	51
D.2	nnU-Net training curves	51
E	SOURCE CODE ACCESS	53

List of Figures

1.1	Anatomy of the coronary tree	1
1.2	Coronary artery disease	2
1.3	Coronary artery tree labeled	4
1.4	Analysis and reporting process of coronary arteries in Hospital de Sant Pau	5
1.5	Pipeline of the complete AI-assisted project for automating CAD diagnosis in Hospital de Sant Pau	8
2.1	Project methodology	9
2.2	Example of ASOCA re-labeling	10
2.3	Centerline extraction pipeline	11
2.4	Skeletonization	12
2.5	Heuristic and topological rule-based method overview	14
2.6	Final heuristic strategy overview	16
3.1	Distribution of cases and segment occurrence in the ASOCA dataset	24
3.2	Distribution of segments per case	24
3.3	Segment distribution in Normal and Diseased cases	24
3.4	Normal and Diseased case examples	25
3.5	Exaple of the underannotated ASOCA segmentations	25
3.6	Ground truth creation	25
3.7	Centerline extraction overview	25
3.8	Bifurcation detection	26
3.9	Heuristic labeling methods for case Normal 1	27
3.10	Coordinate-based ML labeling for case Normal 16	28
3.11	Graph features-based labeling	29
3.12	Feature importance analysis using graph-based Logistic Regression	29
3.13	Segment transition detection results	30
3.14	GraphSAGE labeling results for case Diseased 9	30
3.15	nnU-Net labeling result	32
A.1	Division of the first three RCA segments	44
A.2	Division of the RCA bifurcation	44
A.3	Segments 3, 4 and 16	44
A.4	Examples of posterior descending arteies	45
A.5	Division of the three LAD segments	46

A.6	Diagonal branches example	46
A.7	Ramus intermedius example	46
A.8	Anatomy of obtuse marginal branches	47
A.9	Right-dominant case	48
A.10	Codominant case	48
B.1	Motion artifact	49
D.1	Loss curves over epochs for RCA GraphSAGE model	51
D.2	Testing accuracy over epochs for RCA GraphSAGE model	51
D.3	Loss curves ver epochs for RCA GraphSAGE model	51
D.4	Testing accuracy over epochs for LCA GraphSAGE model	51
D.5	Training curves of nnU-Net per fold	52

List of Tables

1.1	Coronary artery segments description	3
2.1	Occurrence of standard coronary artery segments in the ASOCA dataset	11
2.2	List of ML classifiers used in the study	19
3.1	Bifurcation angles between adjacent segments	26
3.2	Curvature values between adjacent segments	26
3.3	ML model accuracy comparison	27
3.4	Classification report coordinate-based RCA	28
3.5	Classification report coordinate-based LCA	28
3.6	Classification report graph features-based RCA	29
3.7	Classification report graph features-based LCA	29
3.8	Classification report RCA segment transition detection	30
3.9	Classification report LCA segment transition detection	30
3.10	Classification report RCA with GraphSAGE	31
3.11	Classification report LCA with GraphSAGE	31
3.12	Per-segment DSC across folds and average	31
3.13	Average DSC per fold for the nnU-Net model	32
C.1	Graph-derived features used for ML coronary segment classification	50

Chapter 1

INTRODUCTION

1.1 Clinical motivation and context

1.1.1 Coronary arteries

The primary organ of the cardiovascular system is the heart, the muscle responsible for pumping oxygen-rich blood and nutrients to the body's tissues, ensuring their proper function. Like any other muscle, the heart requires its own blood supply to operate optimally, a task carried out by the vessels called coronary arteries.

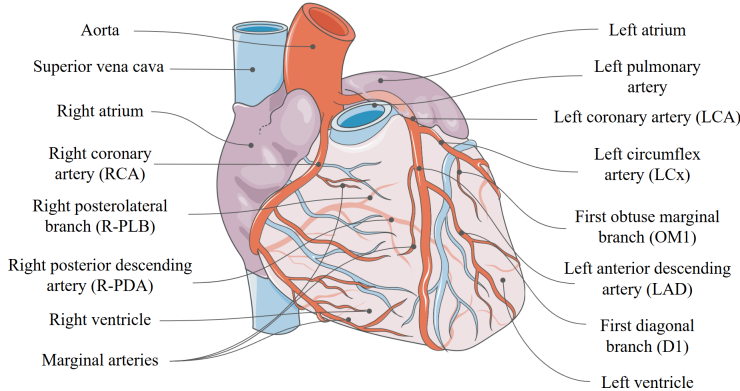


Figure 1.1: Anatomy of the coronary tree, with coronary arteries labeled. Adapted from Servier Medical Art [1].

The coronary arteries are the vascular structures responsible for nourishing the heart muscle, known as the myocardium. As illustrated in Figure 1.1, these arteries originate from the aortic root, the main artery of the body, and encircle the heart like a crown, which is where their name comes from. They are divided into two main branches: the left coronary artery (LCA), which splits into the left anterior descending artery (LAD) and the circumflex artery (LCx), and the right coronary artery (RCA) [2]. These branches further subdivide into smaller vessels that extend throughout the myocardium, delivering oxygen and nutrients to its various regions and enabling the heart to pump blood efficiently to the rest of the body. Importantly, these vessels are not interconnected; a problem in a proximal branch (an early segment closer to the artery's origin) affects the downstream vessel directly.

Understanding the anatomy and function of the coronary arteries is crucial for accurate disease detection and the development of effective treatments. The following sections explore the pathological processes underlying coronary artery disease as well as the segmental anatomy of the coronary artery tree.

1.1.2 Coronary artery disease

Coronary artery disease (CAD) refers to the narrowing or blockage of the coronary arteries, which impairs their ability to deliver sufficient oxygen-rich blood and nutrients to the heart. This condition is called stenosis and develops over time due to the gradual buildup of plaque—a substance composed of fats, cholesterol, calcium, and other components—on the walls of the arteries, a process known as atherosclerosis [3]. Common symptoms of CAD include chest pain, fatigue, shortness of breath, and in severe cases, heart attack. Figure 1.2 illustrates this medical condition.

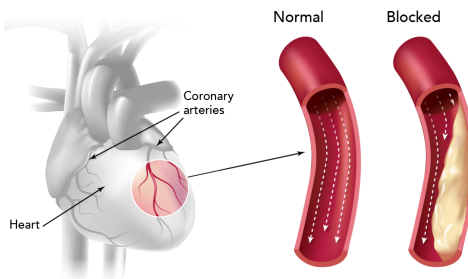


Figure 1.2: Coronary artery disease illustration. From Kaiser Permanente, 2025 [4].

There are two types of CAD: stable ischemic heart disease, where the arteries progressively narrow, and acute coronary syndrome, in which plaque in the arteries suddenly ruptures, forming a clot that obstructs blood flow to the myocardium, leading to a heart attack [5]. CAD is the leading cause of mortality worldwide, responsible for approximately 13% of total deaths each year, as reported by the World Health Organization (WHO) in 2021 [6]. According to the European Society of Cardiology (ESC), cardiovascular diseases in EU account for over 3 million fatalities annually (ESC Atlas, 2024) [7]. In Spain, ischaemic heart disease was responsible for 27,734 deaths in 2023, as reported by the Instituto Nacional de Estadística (INE) [8].

For this reason, it is crucial to promptly identify the disease severity and extension. Early detection of CAD enables clinicians to implement effective treatments that can manage symptoms, slow disease progression, and reduce the risk of life-threatening events.

1.1.3 Coronary artery segments

When identifying the severity of CAD, it is crucial to know the exact location of the pathology. The Society of Cardiovascular Computed Tomography (SCCT) provides a widely used scheme for dividing and classifying the coronary tree [9]. This description is based on the model developed by the American Heart Association (AHA) in 1975 [10], which defines 18 segments.

The RCA is divided into proximal, medial, and distal segments, followed by the posterior descending artery (R-PDA) and the posterolateral branches (R-PLB). The left main coronary

artery gives rise to the LAD, the LCx, and the ramus intermedius (RI). The LAD is further subdivided into proximal, medial, and distal segments, along with the main diagonal branches (D1 and D2). Meanwhile, the LCx includes the proximal and distal segments, the obtuse marginal branches (OM1 and OM2), the left posterior descending artery arising (L-PDA), and the left posterolateral branches (L-PLB), comprising a total of 18 anatomical segments. Table 1.1 outlines the definition of each of the 18 segments according to the SCCT and Figure 1.3 shows an example of the distribution of segments in a real case.

Table 1.1: Numerical identification, name, abbreviation, and description of coronary artery segments. Adaptation from Leipsic, J. *et al* [9]

Number	Segment name	Abbreviation	Description
1	Proximal RCA	pRCA	Ostium of the RCA to one-half the distance to the acute margin of heart
2	Medial RCA	mRCA	End of proximal RCA to the acute margin of heart
3	Distal RCA	dRCA	End of mid RCA to origin of the PDA
4	Right posterior descending artery	R-PDA	PDA originating from RCA
16	Right posterolateral branch	R-PLB	PLB originating from RCA
5	Left main coronary artery	LM	Ostium of LM (left main) to bifurcation of LAD and LCx
6	Proximal LAD	pLAD	End of LM to the first large septal branch or D1, whichever is most proximal
7	Medial LAD	mLAD	End of proximal LAD to one-half the distance to the apex
8	Distal LAD	dLAD	End of mid LAD to end of LAD
9	First diagonal branch	D1	First diagonal branch D1
10	Second diagonal branch	D2	Second diagonal branch D2
11	Proximal LCx	pLCx	End of LM to the origin of the OM1
12	First obtuse marginal branch	OM1	First OM1 traversing the lateral wall of the left ventricle
13	Medial and distal of LCx	LCx	Traveling in the AV groove, distal to the first obtuse marginal branch to the end of the vessel or origin of the L-PDA
14	Second obtuse marginal branch	OM2	Second marginal OM2
15	Left posterior descending artery	L-PDA	PDA originating from LCx
17	Ramus intermedius	RI	Vessel originating from the left main between the LAD and LCx in case of a trifurcation
18	Left posterolateral branch	L-PLB	PLB originating from LCx

It is important to note that the RI is present in only 30% of the cases, while segments 15 and 18 are exclusively present in the cases of left dominance. Coronary dominance refers to the artery supplying the PDA and PLB. Right dominance occurs in 70–80% of the population, codominance in 10–20%, and left dominance in approximately 5–10% [11].

Dividing the coronary arteries according to the anatomy of their branches is essential for accurately locating the disease, assessing its severity, and making therapeutic decisions. For instance, a critical stenosis in a proximal segment can compromise blood flow to large regions

of the myocardium, leading to severe ischemia. In contrast, a lesion in a distal branch (a segment located further away from the artery's origin) would affect smaller myocardial territories, resulting in a less significant clinical impact.

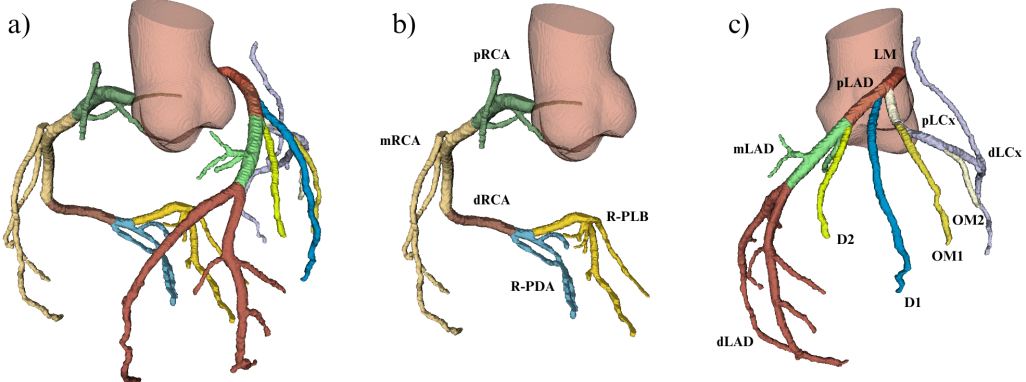


Figure 1.3: Coronary artery tree labeled according to the 18 standard SCCT segments. Case Normal 10 of the publicly available ASOCA dataset [12]. (a) The complete coronary tree, including the aorta. (b) The RCA, annotated with the labels of its respective segments. (c) The LAD and LCx, annotated with the labels of their respective segments. Abbreviations for each segment correspond to those listed in Table 1.1.

1.2 Clinical challenges at Hospital de la Santa Creu i Sant Pau

1.2.1 Diagnostic workflow and associated limitations

The current diagnostic workflow for CAD at Hospital de la Santa Creu i Sant Pau (Hospital de Sant Pau) is complex and time-consuming, which causes cardiologists to spend considerable time on repetitive and manual tasks, instead of focusing on treating critical cases that require their expertise. In particular, the CAD diagnosis begins with the acquisition of coronary CT angiography (CCTA), followed by manual analysis of the scans using the syngo.via software (Siemens Healthineers, Erlangen, Germany) [13]. This analysis is conducted semi-automatically, assisted by tools that enable arterial segment differentiation, stenosis calculation, and plaque evaluation. In addition to coronary analysis, experts review extracardiac and cardiac structures visible in the images. This process can take between twenty minutes and one hour, depending on the case complexity and image quality. The findings are then manually entered into the internal-use platform Filemaker, which generates a preliminary text report. This report is reviewed and corrected by the cardiologist, then finalized and integrated into the Radiology Information System (RIS), after which it is assessed by the referring clinician to determine the subsequent clinical steps.

The overall process faces significant operational challenges, including a lack of prioritization of critical cases, a heavy dependence on expert input, and limited automation. In particular, segment labeling remains a time-consuming and manual task that relies on cardiologist expertise, despite the availability of semi-automatic tools. This dependence, combined with a high volume

of low-risk cases, leads to long delays for imaging and consultations. Given the outlined issues, contributing to the automation of the hospital workflow could significantly support clinicians in accelerating the CAD diagnostic process and ultimately saving lives.

1.2.2 Coronary segment identification

The identification of coronary artery segments plays a fundamental role in clinical decision-making for CAD diagnosis and management. At Hospital de Sant Pau, this process is performed manually by cardiologists using the commercial software syngo.via, which enables detailed visualization of the coronary artery branches, allowing for an in-depth analysis. Although the software includes a semi-automated tool that suggests segment labels, it serves only as a rough guide, and its accuracy depends entirely on the quality of the preceding automated segmentation. Therefore, cardiologists must still visually inspect the vessels, identify bifurcations, and assign labels based on their anatomical knowledge and clinical expertise.

As previously mentioned, this manual process is time-consuming, often requiring between twenty minutes and one hour per patient, depending on the complexity of the case. Experts analyze each vessel in detail, determine the degree of disease for each segment, and extract relevant medical information, such as vessel characteristics and any other findings critical for the diagnosis. Once the analysis is completed, the findings are manually entered into a custom database built on the Filemaker platform, which automatically generates a template-based preliminary report from the introduced data. The doctors then review and correct this generated text, ensuring its accuracy and completeness. Once finalized, the report is integrated into the RIS. Figure 1.4 illustrates this workflow.

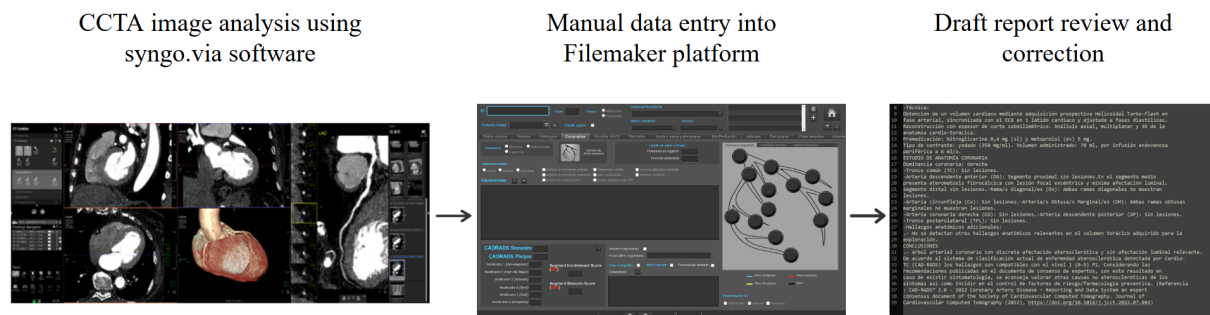


Figure 1.4: Analysis and reporting process of coronary arteries in Hospital de Sant Pau using syngo.via software and the Filemaker platform.

This manual task consumes time that could be more effectively allocated to reviewing complex cases requiring urgent clinical attention. For this reason, automating the process of labeling the standard coronary artery segments from CCTA images has the potential to streamline the CAD diagnostic workflow, reduce time per patient, and enhance the efficiency and consistency of clinical decision-making.

1.3 State of the art: overview of existing automatic coronary labeling approaches

In light of the challenges observed in current clinical practice, significant advances have been made since 2012 in the automatic labeling of coronary artery segments, driven by the incorporation of artificial intelligence (AI), including deep neural networks (DNN), graph modeling techniques, and explicit anatomical knowledge. This section presents a structured review of the main approaches, grouped according to their predominant methodological strategy. Except for the last category, all methods assume that 3D binary masks of the coronary artery tree are provided as input.

Hierarchical and topology-based models

One of the most relevant advancements in recent years has been TopoLab [14], a framework that preserved vascular topology by classifying pairs of connected arterial segments. This strategy prevented labeling errors that were inconsistent with anatomical structure. The system employed a hybrid architecture, combining a Transformer [15] for intra-segment representation and Graph Convolutional Networks (GCNs) for inter-segment modeling, achieving a significant topological consistency of the labeling. On a dataset comprising 72 patients, TopoLab achieved a mean F1-score of 0.87 across cross-validation test folds. On a large in-house dataset with 1,200 patients, the method reached a mean F1-score of 0.92, also averaged across the test folds.

Along the same line, the Neural Syntax Parser [16] addressed the problem from a grammatical perspective. Inspired by natural language syntax parsing, this approach explicitly modeled the hierarchical relationships between segments using grammatical rules trained with neural networks. The model provided an interpretable structure and enabled the integration of clinical preferences without the need for retraining. On a dataset of 1,142 patients, the Neural Syntax Parser achieved a mean F1-score of 0.94, with a mean precision of 0.93 and recall of 0.94, averaged across all vessel categories on the test set.

Graph-structured models

Among graph-based proposals, CPR-GCN [17] stood out by integrating anatomical and visual features extracted from CCTA images through a combination of 3D Convolutional Neural Networks (CNN) and Bidirectional Long Short-Term Memory (BiLSTMs). This hybrid architecture demonstrated high robustness against incomplete data and anatomical variability. On a dataset of 511 patients, the CPR-GCN model achieved a mean F1-score of 0.96, with a mean recall of 0.96 and a mean precision of 0.95, as averaged across all vessel categories in five-fold cross-validation.

Similarly, TreeLab-Net [18] employed a bidirectional TreeLSTM architecture, propagating information from the root to the leaves and vice versa. A key aspect of this method was the transformation of coronary arteries into spherical coordinates (SCT2D), enabling a homogeneous spatial representation across patients and improving the model's ability to capture geometric relationships between arterial branches. On a dataset of 436 patients, TreeLab-Net achieved a mean F1-score of 0.87, as averaged across all vessel categories in tenfold cross-validation.

Spatial and morphological representation approach

The CorLab-Net model [19] introduced a novel approach by incorporating information from the cardiac environment, using anatomical and morphological distance fields to model relationships between vessels and structures such as ventricles and atria. This strategy, complemented by GCNs to reinforce local coherence, demonstrated robust performance, particularly in anatomically complex or distal vessel regions. On a dataset of 100 patients, CorLab-Net achieved a mean F1-score of 0.95, with a mean precision of 0.96 and recall of 0.94, as averaged across all vessel categories in five-fold cross-validation.

Hybrid approach with clinical rules

In addition to purely data-driven approaches, some studies relied on anatomical models and clinical rules. An example was the method by Yang *et al.* [20], which employed a 3D statistical model of the coronary tree and adjusted labels using key bifurcations and clinical criteria. Although more traditional, this rule-based method offered an alternative that prioritized anatomical plausibility and computational simplicity. On a dataset of 58 patients with right-dominant coronary anatomy, only 4.8% of the automatically assigned labels required correction by an expert, and the method achieved an average overlap of 0.91 with reference labels.

Segmentation and labeling from medical images

Finally, certain methods addressed the task as a direct multi-class segmentation problem from CCTA images, where each class represented a distinct coronary segment. Notable examples included the approaches by Ren *et al.* [21] and Shahzad *et al.* [22], which tackled the problem from an arterial wall segmentation perspective. These methods employed 3D U-Net architectures [23] and spatial transformations to locate and label arteries directly from images. In a cohort of 157 patients, the approach by Ren *et al.* achieved an overall accuracy for label presence of 0.96 and an average overlap of 0.94 with reference labels. In the study by Shahzad *et al.*, evaluated on a multi-center dataset of 30 cases, the method achieved a Dice coefficient of 0.68 for healthy and 0.65 for diseased vessel segments. These strategies demonstrated effective alignment with expert annotations in primary vessel regions, although they still faced challenges in secondary and tertiary branches due to anatomical complexity and image variability.

1.4 Project scope and contributions

To address the limitations mentioned in Section 1.2.1, Acebes Pinilla (2023) [24] introduced a structured set of goals to establish an AI-enabled diagnostic framework in the cardiac imaging unit at Hospital de Sant Pau, targeting the improved detection and evaluation of CAD. This project aims to automate and optimize the clinical workflow by reducing specialist workload, streamlining the diagnosis of CAD, and prioritizing the most critical cases.

The complete project consists of five automated stages: segmenting the coronary arteries from CCTA images into a 3D binary mask, labeling the branches of the segmentation into the 18 standard segments, quantifying disease severity and extension in each segment, generating reports of the results, and creating a case priority queue based on the severity of CAD. Figure 1.5 illustrates the entire project scope.

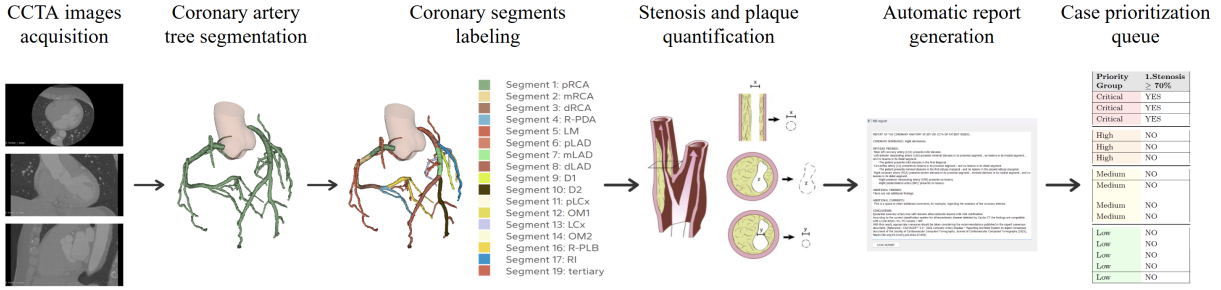


Figure 1.5: Illustration of the pipeline for the ongoing project at Hospital de Sant Pau aimed at automating the diagnosis of CAD through AI-assisted technology. The stenosis and plaque quantification image is adapted from [25]. Automatic report generation and case prioritization queue images are adapted from Ferrer Beltrán [26].

This project has been under development since 2024. During this time, Acebes Pinilla has focused on developing topology-preserving methods to accurately segment the coronary arteries from CCTA medical images [27]. In parallel, Ferrer Beltrán developed automatic preliminary case reports using patients' clinical data and findings derived from CCTA images, in addition to implementing the patient prioritization queue [26].

1.5 Objectives

The objective of this thesis is to design and develop different approaches capable of automatically labeling the 18 standard segments of the coronary arteries, following clinically established criteria. This goal requires a deep understanding of coronary artery anatomy and the creation of a clinically validated dataset, consisting of labeled coronary trees and their corresponding centerlines. Building on this foundation, a key aspect of the project is to analyze the performance and limitations of the different approaches, evaluating their suitability for clinical applications. Ultimately, this work aims to contribute to the development of AI-assisted tools that support the clinical diagnosis of CAD at Hospital de Sant Pau, in order to reduce cardiologists' workload. For the purposes of this study, it is assumed that the coronary artery segmentation step has already been completed.

Chapter 2

METHODOLOGY

2.1 Workflow overview

The methodology of this thesis was divided into two main phases. The first phase involved creating the ground truth dataset required for training and evaluating the models, following established clinical standards. The second phase focused on exploring different approaches for the automatic labeling of coronary artery segments, assessing their performance and limitations in a clinical context. Methods included geometry-based heuristics, rule-based systems (some incorporating the anatomical context of the cardiac chambers), classical machine learning, graph neural networks, and direct multi-class segmentation from CCTA images. Figure 2.1 provides a visual overview of the methodology, and the subsequent sections offer a detailed description of each phase.

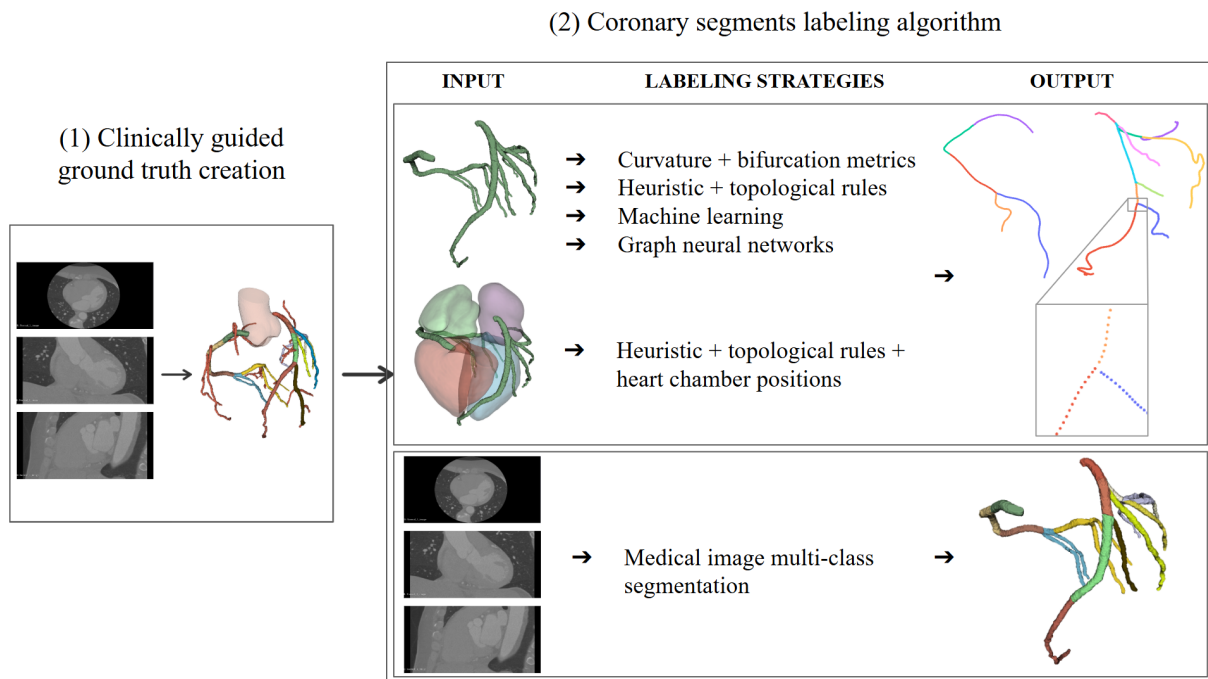


Figure 2.1: Project methodology. (1) illustrates the creation of the labeled dataset. (2) presents the labeling strategies developed, grouped into two types: segmentations as input and point representation as output, and medical images as input and multi-class segmentation as output.

2.2 Coronary segments dataset

2.2.1 Clinically-guided ground truth creation

A dataset of coronary arteries annotated by segments in accordance with established clinical standards was essential for this project, as it provided the necessary ground truth for training and evaluating labeling algorithms. However, no publicly available dataset with these characteristics currently exists. To overcome this limitation, a coronary segments dataset was created manually through a process that combined anatomical study, expert validation, and iterative correction.

The training set from the publicly available Automated Segmentation of Coronary Arteries (ASOCA) challenge dataset [28] was selected as the foundation for this work. This dataset comprises 40 coronary CCTA images along with their corresponding arterial segmentations. The labeling process was conducted using 3D Slicer [29], a medical imaging platform that enables accurate manual annotation of anatomical structures. Each case in the dataset was re-annotated in accordance with the 18-segment standard defined by the SCCT, ensuring consistency with clinical guidelines (see Appendix A for a detailed description of the labeling criteria). The resulting annotations were subsequently reviewed and validated by clinical experts from Hospital de Sant Pau. An example of this process is shown in Figure 2.2.

To reflect clinical priorities, the 18 standard segments were grouped into three categories: primary, secondary, and tertiary. The six main vessels (pRCA, mRCA, LM, pLCx, pLAD, and mLAD) were classified as primary due to their role in perfusing large myocardial regions. The remaining 12 were labeled as secondary, while non-standard branches were designated as tertiary (label 19). This categorization highlights that obstructions in primary segments pose greater clinical risk, whereas distal or tertiary lesions generally have less immediate impact.

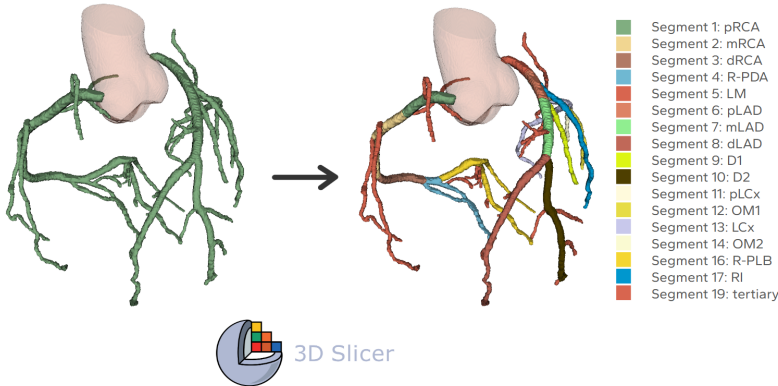


Figure 2.2: Example of manual re-labeling performed on case Normal 10 from the ASOCA dataset, using 3D Slicer [29].

It is important to highlight that the ASOCA dataset, despite being one of the most commonly used resources for coronary artery segmentation, has significant limitations. The dataset consists of only 40 cases (20 healthy named "Normal" and 20 with CAD named "Diseased") and lacks a balanced distribution of the standard coronary segments, as shown in Table 2.2.1. In particular, segments 15 and 18 are entirely absent because all cases exhibit right coronary dominance. While right coronary dominance is common, occurring in approximately 70–80% of the population [11], this anatomical bias reduces the dataset's representativeness and limits its

potential for generalization. Furthermore, the segmentations exhibited notable incompleteness, as although the segments were present, their lengths were often incorrect, resulting in discrepancies in anatomical continuity. Additionally, some images were affected by imaging artifacts, such as motion shift, which further complicated both the re-labeling process and subsequent evaluation.

Table 2.1: Number of cases in the ASOCA dataset containing each standard coronary artery segment. Segments marked with * are absent due to right coronary dominance.

Segment	1	2	3	4	5	6	7	8	9	10	11	12	13	14	15*	16	17	18*
Cases	40	40	40	32	40	40	40	40	32	26	39	19	39	15	0	31	15	0

2.2.2 Centerline extraction

Once the re-labeled dataset was created, most of the labeling strategies described in this thesis required extracting centerlines from the input data. These inputs consisted of 3D segmentations of the complete coronary artery tree in NIfTI format. To obtain the centerlines, a common three-step preprocessing pipeline was applied, as illustrated in Figure 2.3 and detailed below.

It is important to note that some methods required additional input features not provided by the general pipeline. For example, the curvature- and bifurcation-based algorithm relied on centerline data with tangent vectors and curvature, extracted using Mimics 27.0 Research Edition (Materialise, Leuven, BE), a software tool for advanced 3D medical image processing and analysis. The specific inputs needed for each method are detailed in their respective subsections.

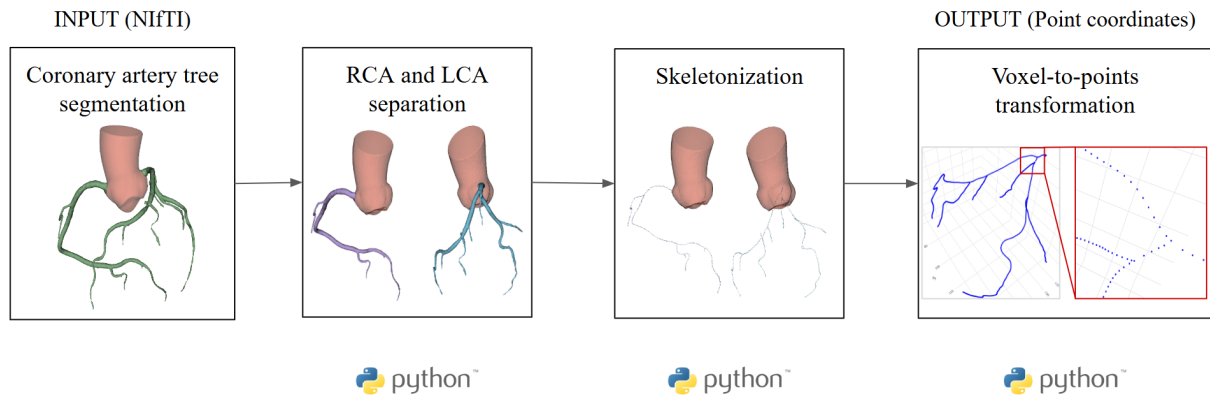


Figure 2.3: Centerline extraction pipeline.

RCA and LCA separation

The complete coronary tree was separated into its two main branches, the RCA and the LCA. This was achieved by identifying the two largest connected components in the segmentation and computing the center of mass for each. The component with the rightmost center of mass was classified as the RCA, and the leftmost as the LCA. Each component was then saved independently for subsequent processing. These operations were implemented leveraging Python libraries, including nibabel [30] for NIfTI file handling and scikit-image [31] for connected

component analysis. This early separation facilitates the application of distinct anatomical rules in the labeling process, given the differing branching patterns of RCA and LCA.

Skeletonization

For each coronary artery (RCA and LCA) and each of their respective segments, the 3D segmentation was converted into a single-voxel-wide centerline that preserved the topology of the original structure. This was achieved by first computing a global skeleton from the binary mask of the entire coronary tree using the 3D skeletonization algorithm provided by the scikit-image library [31]. Subsequently, the binary masks of each labeled segment were extracted, and their voxel-by-voxel intersections with the global skeleton were computed. This approach ensured continuity between adjacent segment centerlines. In contrast, skeletonizing each segment independently would have led to disconnected or misaligned endpoints due to segmentation boundaries. Figure 2.4 illustrates this procedure.

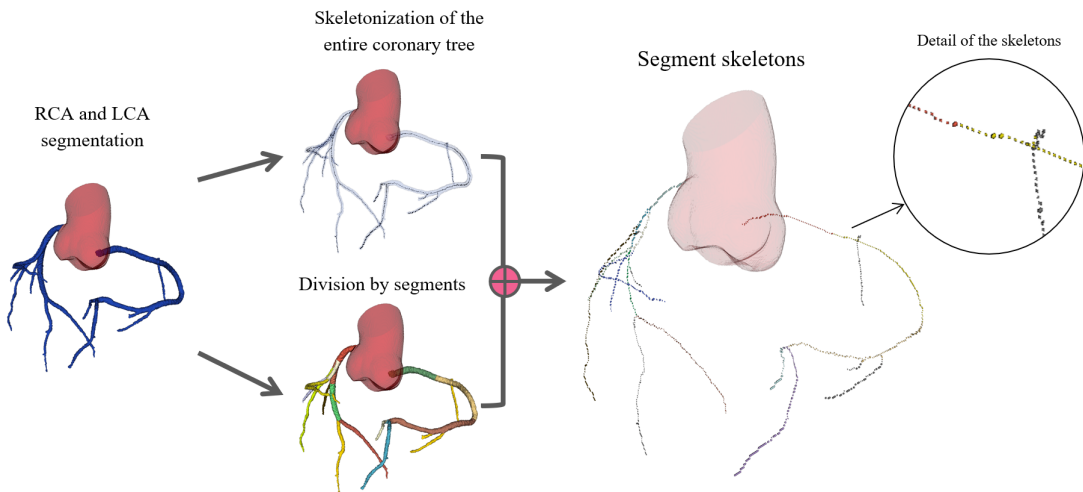


Figure 2.4: Skeletonization by segments procedure. Adapted from Acebes Pinilla.

Voxel-to-points transformation

Once the skeletonized representation of the coronary arteries was obtained, the resulting voxels were converted into points expressed in real-world coordinates (in millimeters). This conversion was performed by processing each coronary segment stored in a NIfTI file. Each file contained a binary image in which voxels with a value greater than zero represented the centerline of the segment. Subsequently, the physical voxel size (i.e., its dimensions in millimeters) was extracted from the NIfTI header, and the three-dimensional coordinates (i, j, k) of all skeleton voxels were identified. Since these coordinates referred to the corner of each voxel, they were adjusted by adding 0.5 to each component so that the resulting point was in the center of the voxel. These centered coordinates were then multiplied by the voxel dimensions to obtain the physical coordinates (P_x, P_y, P_z) in millimeters. This adjustment aligns with the convention described in the Insight Segmentation and Registration Toolkit (ITK), where the center of a voxel is located at offset (0.5, 0.5, 0.5) from its index coordinate [32]. The transformation applied to each voxel coordinate is mathematically expressed as:

$$(P_x, P_y, P_z) = (i + 0.5, j + 0.5, k + 0.5) \times \text{voxel_size} \quad (2.1)$$

This simplified transformation assumed that the origin of the real-world coordinate system coincided with the image origin (0, 0, 0). This approach is a standard in medical imaging libraries such as ITK and SimpleITK [33], ensuring geometric consistency between voxel indices and physical space. The resulting points for each segment were stored in a DataFrame along with their corresponding labels.

2.3 Geometry- and structure-based labeling strategies

In this section, two distinct heuristic algorithms are presented for each strategy: one designed for the RCA and another for the LCA. These algorithms assume that the input consists of centerlines of a pre-segmented coronary artery tree, with no tertiary branches included.

2.3.1 Curvature and bifurcation method

The first heuristic approach explored was based on the local geometry of the coronary artery centerlines, with a focus on identifying segment boundaries through bifurcations and abrupt changes in curvature. This strategy was designed in alignment with clinical guidelines and expert input from cardiologists at the Hospital de Sant Pau, who highlighted these two anatomical features as the most relevant criteria for distinguishing coronary segments.

To apply this method, centerlines were extracted from the segmented coronary trees using Mimics, which provided the tangent vector and curvature value at each point. These geometric descriptors were then used to assign segment identifiers based on significant morphological changes. Specifically, a new segment label was assigned whenever the angle between consecutive tangent vectors exceeded 35° , or when the curvature surpassed a predefined threshold (ranging from the empirically computed values of 0.06335 to 0.1846125, depending on the segment pair). These thresholds were established by analyzing typical transitions and bifurcations in representative cases from the dataset.

The experiments began with a subset of four cases selected for their high number of segments and to ensure a balanced distribution of 50% healthy and 50% diseased samples: Normal 1, Normal 7, Diseased 7, and Diseased 9. Starting with this small set enabled a gradual and controlled evaluation of the method, allowing issues to be identified and adjustments to be made before considering a broader dataset. After extracting the centerlines for these four cases, bifurcation angles and curvature values between consecutive segments were computed and stored for subsequent analysis. While the method achieved a correct differentiation of bifurcation points, it exhibited a strong dependency on the ordering of the input data. Given these limitations and the insights obtained, detailed in the Discussion section, the approach was ultimately discarded, and further exploration of alternative methods was prioritized.

2.3.2 Heuristic and topological rule-based method

Building upon the insights and limitations observed in the curvature and bifurcation strategy, this second approach was devised to improve the reliability of labeling coronary segments,

especially at bifurcation points. It labeled the centerlines of coronary arteries by applying a set of heuristic and topological rules based on the arteries' orientation, branching structure, and bifurcations. The input consisted of tabular data containing the three-dimensional coordinates (P_x, P_y, P_z) in millimetres for each point along the centerline. The algorithm processed this data through a sequence of geometric transformations and decision rules, ultimately generating an output DataFrame in which each point was annotated with its corresponding anatomical segment label. Figure 2.5 illustrates an overview of the methodology followed in this section.

To enable a robust structural analysis, the centerlines were represented as undirected graphs, where:

- Each point is modeled as a node.
- Connections between adjacent points are modeled as edges.
- Each node is connected to its previous and next neighbors.
- Nodes with more than two connections indicate a bifurcation.

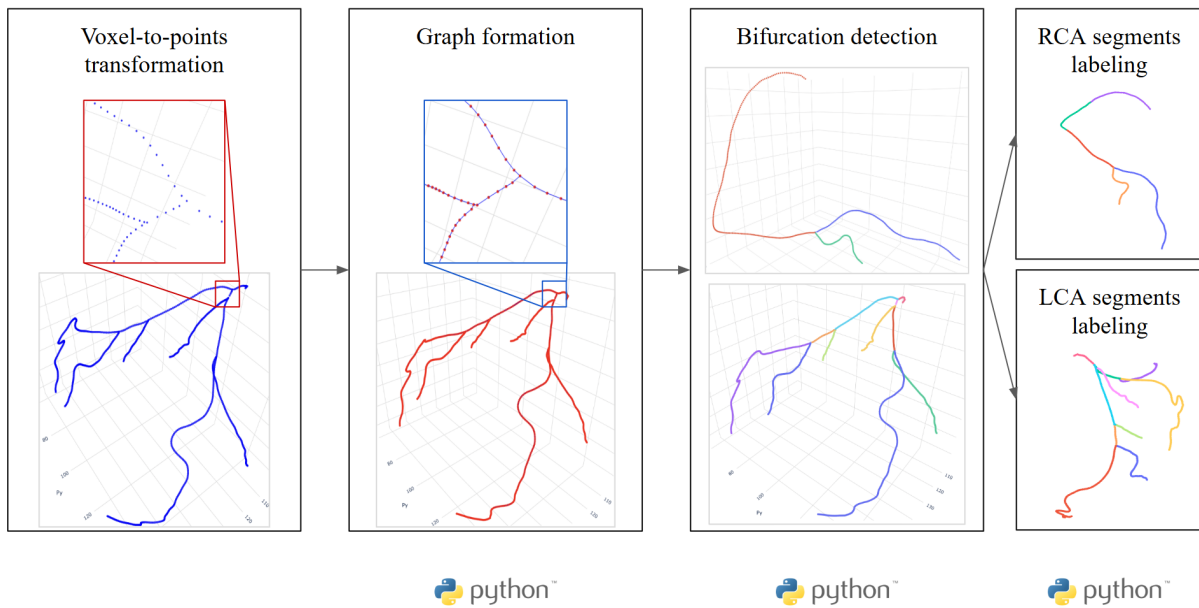


Figure 2.5: Heuristic and topological rule-based method overview.

Graph formation

The first step involved constructing a graph from the set of centerline points. To enforce a tree-like structure (i.e., a connected graph without cycles), the classical algorithm from graph theory called Minimum Spanning Tree (MST) was generated. The MST guarantees that all nodes are connected by edges of minimal total distance, ensuring a unique and cycle-free representation of the coronary artery tree.

The MST was constructed as follows:

1. The Euclidean distance matrix between all points was computed using their three-dimensional coordinates (P_x, P_y, P_z).

2. A complete undirected graph was created, where each point was represented as a node, and an edge was added between every pair of nodes. The weight of each edge was defined by the corresponding entry in the distance matrix.
3. The MST was extracted from this complete weighted graph using Kruskal's algorithm, as implemented in the NetworkX library [34].

Bifurcation detection

Once the graph was constructed, bifurcations were identified by iterating over all nodes and checking their degree of connectivity. Nodes with more than two connections were classified as bifurcation points, corresponding to anatomical locations where the artery split into branches. In addition, the root node was defined as the leaf node (with a single neighbor) located at the highest P_z . Starting from this root, the subsequent labeling of arterial segments was performed by traversing the graph, using the detected bifurcations, and applying topological rules specific to each coronary artery, as detailed in the following sections.

RCA segments labeling

From the root node, a breadth-first search (BFS) was performed until the first bifurcation was reached. The path from the basal node to this bifurcation was divided into three equal parts, which were labeled as segments 1 (pRCA), 2 (mRCA), and 3 (dRCA), representing the proximal, medial and distal sections of the RCA.

After locating the bifurcation, its two child branches were identified. The branch whose initial node had a lower P_z value (the one that descended in a downward direction) was classified as the R-PDA and labeled as segment 4. The other branch, which had a more lateral orientation (higher P_z), was labeled as the R-PLB, corresponding to segment 16. Each of these branches were then labeled by propagating the respective segment identifier through a depth-first search (DFS), avoiding backward traversal to the previous bifurcation.

LCA segments labeling

In the case of the LCA, the process was more complex due to its more extensive branching. It also began from the root node, from which a BFS was executed to locate the first bifurcation. The path leading to this first bifurcation was labeled as segment 5 (LM).

After this bifurcation, the two child branches were analyzed based on their P_y coordinates: the branch with the lower P_y value (more anterior) was classified as segment 6 (pLAD). Two new branches emerged from this point: the one that descended further (lower P_z) was labeled as segment 7 (mLAD), and the other as segment 9 (D1). Their respective labels were propagated along each branch. If a new bifurcation was detected along segment 7, The P_z values of its children were compared: the more apical branch (lower P_z) was labeled as segment 8 (dLAD), and the other as segment 10 (D2).

Meanwhile, the second main branch arising from the bifurcation at segment 5 corresponded to the LCx, which was labeled as segment 11. Three successive bifurcations were identified along this branch. The first split the branch into segments 11 and 17 (RI), based on the P_x coordinate:

the child node with the higher P_x (more lateral) corresponded to segment 17. The continuation of the LCx led to a second bifurcation, whose branches were labeled as segments 12 (higher P_x) and 13 (lower P_x). A third bifurcation was then identified, and its branches were labeled as segments 14 (higher P_x) and 15 (lower P_x).

All of this labeling was performed via DFS traversals from the bifurcation nodes into their respective branches, propagating the segment identifiers based on their relative position in 3D space.

2.3.3 Final heuristic-based method

In order to overcome the limitations of the previous method, which are examined in the Discussion section, a second heuristic and topological rule-based labeling algorithm was developed. Nevertheless, this approach leveraged the spatial proximity between coronary arteries and cardiac chambers (the ventricles, atria, and the apex) to assign anatomical segment labels. Unlike the previous topology-only approach, this method does not depend on fixed axes but also takes into account the orientation and spatial arrangement of the heart within the thorax, adding robustness when the heart is rotated or displaced. Figure 2.6 illustrates this approach, which is detailed below.

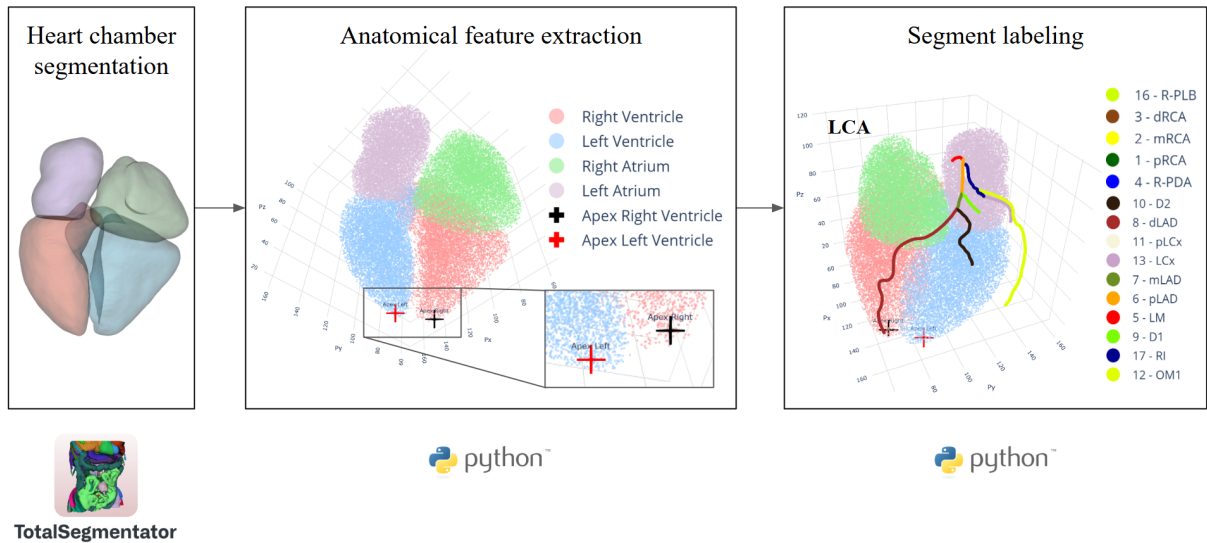


Figure 2.6: Final heuristic strategy pipeline.

Heart chambers segmentation

For each case in the dataset, the segmentation of the cardiac chambers was extracted from the CCTA images using the "heartchambers_highres" task of TotalSegmentator [35]. This framework enabled the automatic identification of multiple anatomical structures directly from CT images. In this case, masks corresponding to the main chambers (right atrium, left atrium, right ventricle, and left ventricle) were generated and saved in NIfTI format.

Heart chambers features extraction

For each chamber, the 3D coordinates of the voxels were extracted using Equation 2.1, and the output was a 3D point cloud for each chamber. Subsequently, to calculate the proximity of these point clouds to each component of the centerline, an efficient data structure for proximity queries, the KD-Tree, was employed. This decision was made because the point clouds contained hundreds of thousands of points, and the KD-Tree significantly accelerated nearest-neighbor searches, reducing the computational cost from $\mathcal{O}(n \cdot m)$ to $\mathcal{O}(n \cdot \log m)$, where n represented the number of artery points and m the number of chamber points.

Once the KD-Trees for all chambers had been built, a nearest-neighbor search was performed for each point of the centerline using the corresponding KD-Tree. This process returned the Euclidean distance to the nearest point of each chamber. These distances were then stored as additional columns in the DataFrame.

Ventricular apex estimation

In addition to the distance to each chamber for every centerline point, the estimated distance to the cardiac apex was also added. To achieve this, the position of the apex was first estimated, followed by the corresponding distance calculations. To estimate the cardiac apex, the convex hull of each ventricular chamber was used. The convex hull is the smallest convex shape that encloses a set of points, and in this context, it was used to define the outer boundary of the chamber. Then, the apex was defined as the point on the convex hull with the smallest value in the Z axis, followed by the Y and X axes. Once estimated, the Euclidean distance from each point of the artery to the apex of both ventricles was calculated, and this information was added as new columns in the DataFrame.

RCA segments labeling

The assignment of labels in this branch followed the same procedure as described in the previous Section 2.3.2, with the unique difference that the bifurcations of the RCA were analysed based on their distance to the apex and the ventricles, rather than by comparing their P_y value. Specifically, the branch closest to the apex of the right ventricle was labeled as segment 4 (R-PDA), whereas the branch nearest to the left ventricle and atrium was labeled as segment 16 (R-PLB).

LCA segments labeling

For this artery, the overall strategy described in Section 2.3.2 was adapted to incorporate anatomical distances in the decision rules. The assignment logic remained unchanged only for segment 5 (LM), which did not depend on positional information and simply extended from the root node to the first bifurcation of the LCA.

To differentiate between the LAD and the LCx, anatomical distances were compared. The branch closest to the right ventricle was assigned as the beginning of segment 6 (pLAD), while the branch nearest to the left atrium was assigned as the beginning of segment 11 (LCx).

The LAD was assigned as segment 6 from its origin to the next bifurcation. At this bifurcation, two branches were detected: the one closer to the right ventricle was labeled as segment 7

(mLAD), and the one closer to the left ventricle was labeled as segment 9 (D1). Subsequently, from the end of segment 7, the algorithm searched for an additional bifurcation. If one was found, two further branches were identified: the one closer to the right ventricle was assigned as segment 8 (dLAD), while the one closer to the left ventricle was assigned as segment 10 (D2). If no bifurcation was found, segment 7 was divided in half, and the second half was labeled as segment 8.

Once the LAD branch had been processed, the LCx segments were addressed. The first segment was labeled as segment 11 (pLCx). At the first bifurcation, the algorithm checked whether the new branch was sufficiently close to the origin (within 8 nodes from the initial node of segment 11); if so, it was labeled as segment 17 (RI), and the other branch was considered a continuation of segment 11. Otherwise, the presence of segment 17 was disregarded, and both branches were considered continuations of segment 11. Next, segment 11 was followed until a second bifurcation was encountered. From this point, segments 12 (OM1) and 13 (LCx) were identified, and the node closest to the apex of the left ventricle was labeled as segment 12, while the node closest to the left atrium was labeled as segment 13. If a third bifurcation was identified, the node also closest to the apex of the left ventricle was labeled as segment 14 (OM2).

2.4 Machine learning-based labeling strategies

After conducting several experiments with the previously detailed heuristic algorithms, it was decided to explore approaches capable of learning these labeling rules automatically. To this end, various supervised machine learning (ML) models were tested. As in previous strategies, the input consisted of centerlines from a pre-segmented coronary artery tree, excluding tertiary branches. The models were trained and evaluated separately for the RCA and the LCA, reflecting their distinct anatomical patterns.

2.4.1 Coordinate-based method

To assess the viability of this strategy, the process began with simple experiments. Meaning that several ML algorithms were evaluated using only the spatial coordinates (P_x, P_y, P_z) of the centerline points as input variables. The objective was to predict the segment number corresponding to each point, treating it as a multiclass classification problem. This approach allowed the establishment of a baseline to evaluate how informative the spatial positions alone could be, while also assessing the overall performance of ML algorithms for this task.

To ensure the validity of the evaluation, stratified splitting was performed by clinical condition, ensuring that no samples from the same case appeared in both training and test sets. Moreover, a 70/30 train-test split was performed at the case level within each clinical group (Normal and Diseased). These details were crucial to prevent overfitting and to ensure a fair assessment in real clinical scenarios.

After this splitting, the coordinates were standardized using z-score normalization, and the segment labels were numerically encoded using the LabelEncoder function from the scikit-learn library [36]. This facilitated the training of the 18 classification models used. For each model, a classifier was trained with the preprocessed centerline data, predictions were generated on the

test set, and performance was evaluated. The selection included both tree-based and non-tree-based models, driven by the initial hypothesis that tree-based algorithms might perform better due to the tree-like structure of coronary arteries. The models used are listed in Table 2.2.

This approach served as an initial exploratory step, enabling the evaluation of the potential of ML for the task of automatic segment labeling. It highlighted that, while the coordinates alone may provide sufficient information in certain cases, there are scenarios where a richer representation of the arterial context is necessary, as will be addressed in the following section.

Table 2.2: List of ML classifiers used in the study. All models were implemented using the scikit-learn library [36], complemented with additional frameworks such as XGBoost [37], LightGBM [38], and CatBoost [39].

Tree-based Models	Non-tree-based Models
Random Forest	Logistic Regression
Gradient Boosting	Perceptron
Extra Trees	Ridge
Extreme Gradient Boosting (XGBoost)	Support Vector Machine (SVM)
Decision Tree	K-Nearest Neighbors (KNN)
Adaptive Boosting (AdaBoost)	Gaussian Naive Bayes
Light Gradient Boosting Machine (LightGBM)	Linear Discriminant Analysis (LDA)
Categorical Boosting (CatBoost)	Quadratic Discriminant Analysis (QDA)
Histogram-based Gradient Boosting	Multi-Layer Perceptron (MLP)

2.4.2 Graph features-based method

In this second approach, structural knowledge of the coronary artery tree was incorporated through features derived from the MST. Unlike the previous method, which solely relied on spatial coordinates, this strategy introduced topological and local geometric information for each point of the tree, allowing the capture of relevant vascular morphology properties.

For each clinical case, an MST was constructed from the 3D coordinates of the centerline points. From this graph, global features were extracted: DFS visit order, the node index within the graph, the Euclidean distance to the origin, the number of neighbors in the MST (degree of the node), the path length to the root node in terms of graph steps (topological depth), and the geodesic distance to the root node along the weighted edges of the MST. This set of features was subsequently combined with the original spatial coordinates, enriching the representation of each arterial point.

As in the previous experiment, stratified splitting by clinical condition was applied, a 70/30 train-test split was performed, variables were standardized using z-score normalization, and the segment labels were encoded numerically. Moreover, the same 18 classification models from the earlier section listed in Table 2.2 were evaluated and the results of this strategy are analyzed in detail in the Discussion section.

2.4.3 Segment transition detection method

In order to explore an alternative labeling strategy, a method oriented towards the detection of transitions between arterial segments was implemented. Unlike the previous approach, in which each point was directly classified into a specific segment, this method aimed to identify solely the points where a change of segment occurred. These points were assigned non-zero values (1, 2, 3, ...), whereas the remaining points were labeled with a neutral class (0). This method redefined the problem as a task of detecting discrete point events rather than performing full segment classification and was also applied separately to RCA and the LCA.

For this purpose, a Logistic Regression classification model was trained using as input features the 3D coordinates (P_x, P_y, P_z) together with the same topological graph descriptors derived from the MST used in the previous approach. This choice was motivated by the promising results obtained in Section 2.4.2, which highlighted the importance of incorporating structural information. Again, all features were standardised using z-score normalization, and the labels were numerically encoded. Further results and analysis are provided in Sections 3 and 4.

2.5 Graph neural network labeling strategy

To exploit the inherent tree-like structure of coronary arteries, a classification strategy based on Graph Neural Networks (GNNs) was explored, with a particular focus on the GraphSAGE model [40]. This approach aimed to explicitly model the spatial relationships between points by incorporating the topological connectivity of the arterial tree, represented as a MST. Specifically, for each clinical case, a graph was constructed where nodes corresponded to the arterial centerline points, and edges represented the connections defined by the MST computed over the 3D coordinates. In this graph structure, each point was labeled with its respective arterial segment identifier, and only the spatial coordinates (P_x, P_y, P_z) were used as input features.

Furthermore, the data were preprocessed and formatted using the PyTorch Geometric library [41], ensuring compatibility with graph-based models. Subsequently, the dataset was split into training and testing sets following an 80/20 ratio to facilitate model evaluation. The GraphSAGE model was then defined with two convolutional layers, an intermediate ReLU activation function, and a final layer that projected to an output space matching the number of segment classes.

Regarding the training process, the model was trained over 600 epochs using the cross-entropy loss as the loss function and the Adam optimizer for parameter updates. Throughout the training process, both loss and accuracy metrics were recorded for training and testing datasets to monitor the model’s performance. This strategy was applied separately to the RCA and LCA in order to evaluate the model’s performance across different anatomical configurations, with training times of approximately 7 minutes each due to the small dataset size and simple graph structures.

2.6 Direct multi-class segmentation strategy

The last stage of the project consisted of training a deep learning model to automatically segment coronary artery segments from CCTA images. For this purpose, the nnU-Net framework (Isensee *et al* 2020), [42] was employed, a self-configuring method that adapts its architecture and training pipeline to a given medical segmentation task without manual intervention. The objective was to leverage a state-of-the-art tool to obtain 3D multiclass segmentations of the standard coronary segments, using the annotated dataset described in the Section 2.2.1.

The input data used in this experiment contained the 40 ASOCA CCTA images, each annotated with 19 coronary artery segments. The input data was formatted according to the nnU-Net structure defined by Isensee *et al*. This included arranging the CCTA images and their corresponding segmentation masks in the correct folder structure and creating a valid JSON descriptor file.

Additionally, a 5-fold cross-validation strategy was employed to ensure robust model evaluation. The model was trained using the 3D full-resolution configuration of nnU-Net, which processes the input volumes at their highest feasible resolution to maximize spatial accuracy. Training was conducted on the Consorci de Serveis Universitaris de Catalunya (CSUC) computing cluster Pirineus III [43], using one GPU per fold. Initially, training was configured for 1000 epochs per fold. However, due to a lack of convergence observed in validation metrics, the training was extended to 2000 epochs. This adjustment aimed to give the model more capacity to optimize, given the complexity of the task and the class imbalance. Training all five folds in parallel took approximately five days to complete.

The final configuration selected by the nnU-Net framework was a 3D full resolution U-Net with six encoding-decoding stages. Each stage consisted of two convolutional blocks using 3D convolutions with kernel sizes of $3 \times 3 \times 3$, instance normalization, and Leaky ReLU activation functions. The number of feature channels per stage increased from 32 to 320, and downsampling was performed using strided convolutions, with strides of $2 \times 2 \times 2$ except in the first and last stages. The model was trained on input patches of size $80 \times 160 \times 160$ with a batch size of 2. CT-specific intensity normalization was applied, and the Dice loss was computed per batch. This architecture was selected automatically by nnU-Net based on the spatial resolution and anatomical complexity of the input data.

2.7 Evaluation

Given the diversity of approaches developed in this project, distinct evaluation strategies were required to suit the specific logic and design of each method. Furthermore, for every approach, visual inspection played a fundamental role in this process, offering essential insights into the behaviour of the algorithms and the anatomical plausibility of the results. The following sections detail the evaluation strategies employed for each category of methods.

Geometry-and structure-based labeling evaluation

As these methods were developed from scratch based on heuristic rules derived from anatomical knowledge, their correctness was evaluated by comparing the algorithm's output with manually annotated ground truth. Each segment was checked to ensure that the assigned labels matched

the expected anatomical locations according to the SCCT standard, with particular attention to key landmarks such as bifurcations and branching patterns.

Machine learning and graph neural network evaluation

The performance of the ML and GraphSAGE classification models was assessed using standard metrics for multi-class classification tasks. Specifically, precision, recall, F1-score, and accuracy were computed for each anatomical segment. These metrics are defined as follows:

$$\text{Precision} = \frac{TP}{TP + FP} \quad (2.2)$$

$$\text{Recall} = \frac{TP}{TP + FN} \quad (2.3)$$

$$\text{F1-score} = 2 \cdot \frac{\text{Precision} \cdot \text{Recall}}{\text{Precision} + \text{Recall}} \quad (2.4)$$

$$\text{Accuracy} = \frac{\text{Number of correct predictions}}{\text{Total number of predictions}} = \frac{TP + TN}{TP + TN + FP + FN} \quad (2.5)$$

In these equations, TP (true positives) denotes the number of samples correctly predicted as belonging to a given segment, while FP (false positives) refers to samples incorrectly assigned to that segment. FN (false negatives) represents samples that truly belong to the segment but were not identified as such by the model. Finally, TN (true negatives) corresponds to samples correctly predicted as not belonging to the segment.

Direct multi-class segmentation evaluation

The nnU-Net segmentation model was evaluated using the Dice Similarity Coefficient (DSC), a widely adopted metric for assessing the overlap between predicted and ground truth segmentations in medical imaging. The DSC values were computed for each of the 18 standard coronary segments and for each fold, enabling a quantitative assessment of the segmentation performance for the nnU-Net model. The DSC is defined as follows:

$$\text{DSC} = \frac{2 \times |X \cap Y|}{|X| + |Y|} \quad (2.6)$$

where X and Y represent the sets of voxels corresponding to the predicted and reference segmentations, respectively. This metric ranges from 0 (no overlap) to 1 (perfect overlap).

Chapter 3

RESULTS

3.1 Dataset creation

As outlined in Section 2.2.1, the widely known public ASOCA dataset presents several limitations. Figure 3.1 illustrates the distribution of cases in the dataset and the presence of each standard segment within it. It can be observed that primary segments appear more frequently than secondary ones, and that the segments 15 (L-PDA) and 18 (L-PLB) are not present in any case. Further insights are provided by Figures 3.2 and 3.3, which display the distribution of segments per case, distinguishing between Normal and Diseased. The number of segment occurrences was highly similar for both case types: there were 266 segment occurrences in the Normal cases and 264 in the Diseased cases. To better illustrate the differences between these two groups, Figure 3.4 presents an example of each. The primary distinction is that Diseased cases, which are affected by CAD and exhibit stenosis, show visible alterations in the shape and continuity of the segmented arteries, such as narrowing or irregularities along the vessel walls. In contrast, the segmentations of Normal cases retain a smoother and more regular morphology.

Additionally, Figure 3.5 shows an example of the incompleteness of the annotations provided by the ASOCA dataset. As can be seen, the original dataset lacks many branches, especially tertiary ones, and the main branches are incomplete. For this project, the ground truth was manually generated from the ASOCA segmentations, following clinical guidelines and with the assistance of experts from Hospital de Sant Pau. The re-labeling was performed using 3D Slicer, and Figure 3.6 shows four examples of the final labeled dataset.

Moreover, as discussed in Section 2.2.2, after the manual re-labeling process, the centerlines of the coronary arteries were extracted from this ground truth to enable subsequent analyses. Figure 3.7 presents an example of the resulting centerlines, which were generated without including tertiary branches. Nevertheless, some anomalies remain apparent in the extracted points.

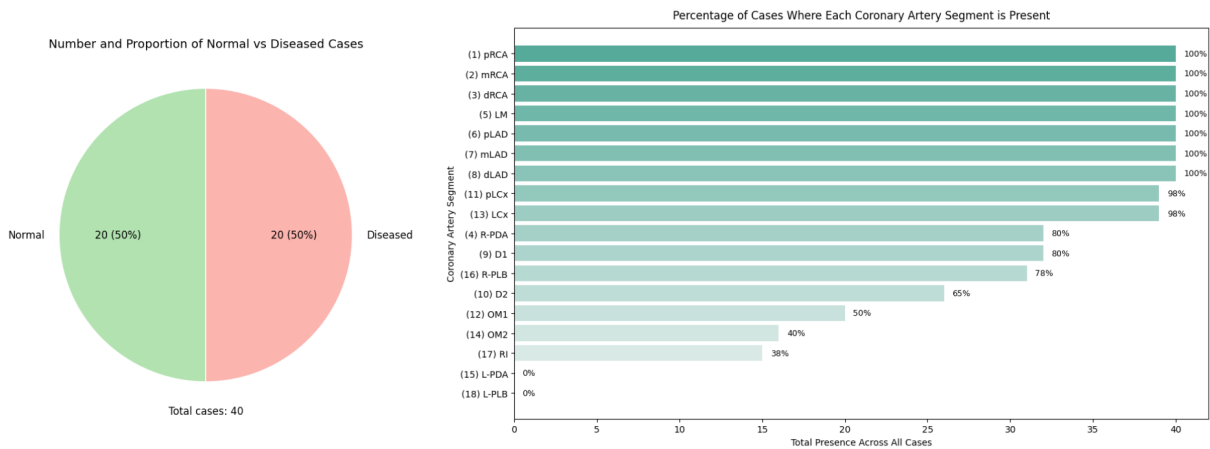


Figure 3.1: Distribution of Normal and Diseased cases (left) and the occurrence of each coronary artery segment (right) in the ASOCA dataset.

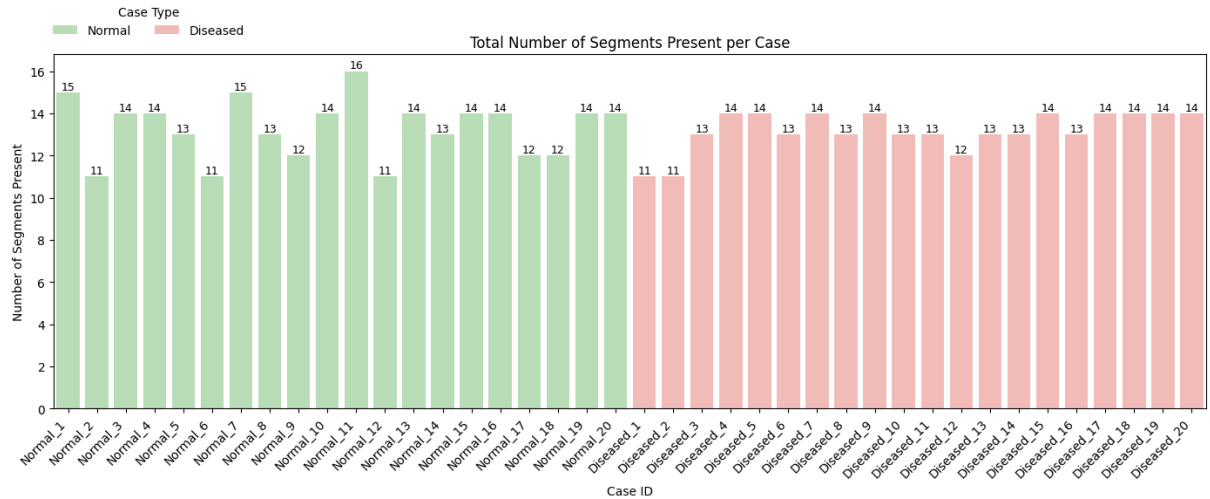


Figure 3.2: Total number of segments present per case.

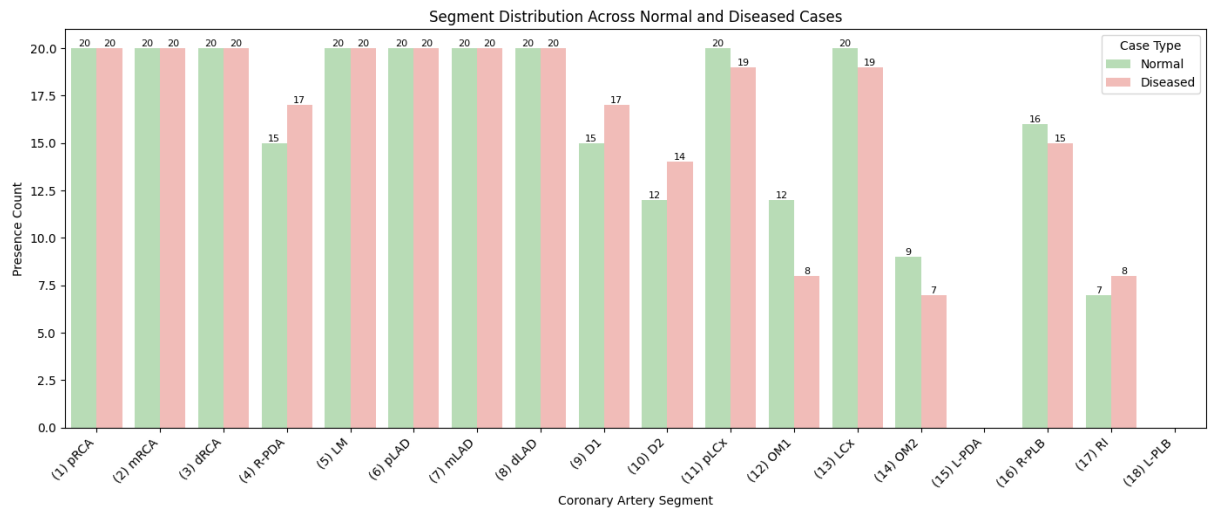


Figure 3.3: Segment distribution across Normal and Diseased cases.

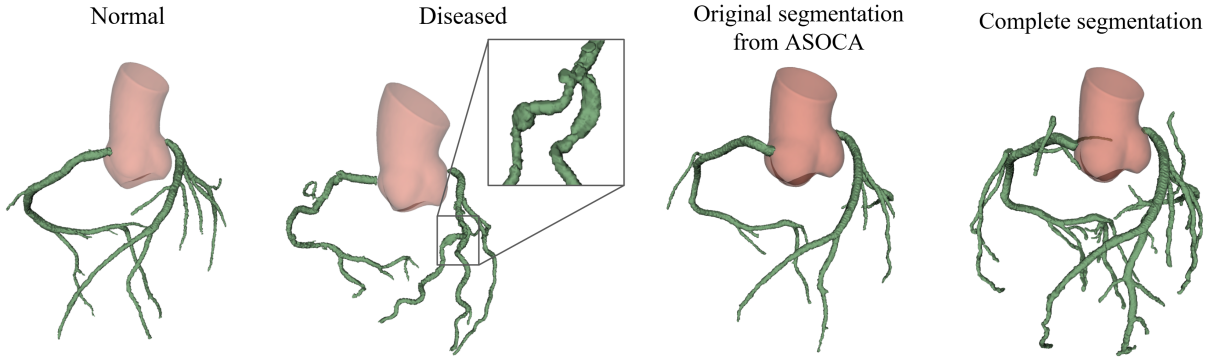


Figure 3.4: Normal (case 3) and Diseased (case 5) examples from the ASOCA dataset.

Figure 3.5: Example of the underannotated ASOCA segmentations (case Normal 10).

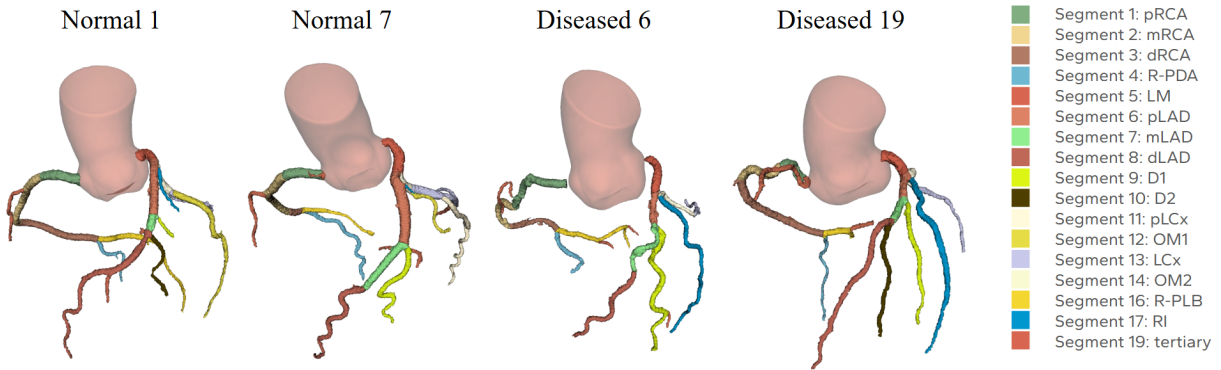


Figure 3.6: Manually re-labeled ASOCA cases based on clinical guidelines.

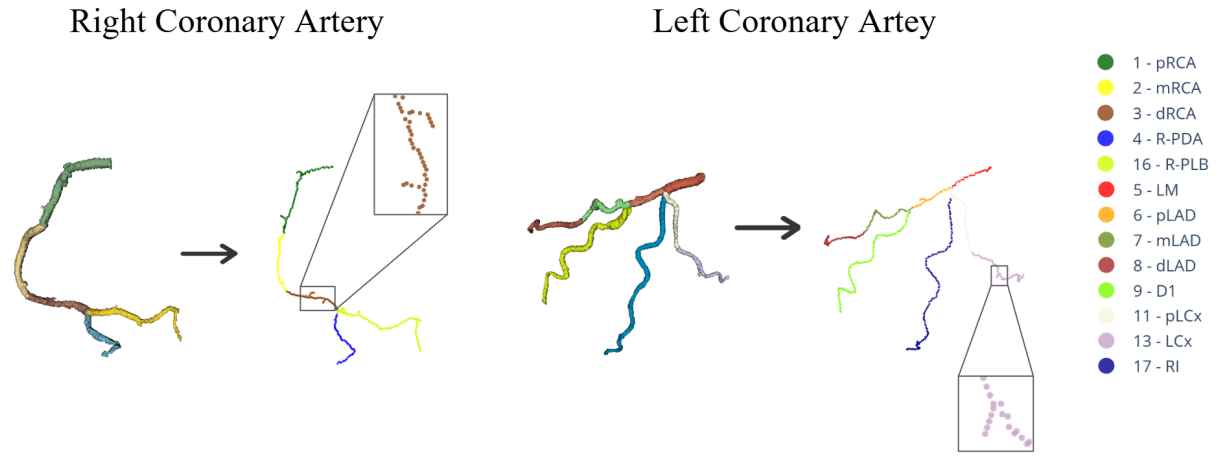


Figure 3.7: Extracted centerlines and their irregularities in ASOCA case Diseased 3.

3.2 Geometry- and structure-based labeling

For the curvature- and bifurcation-based labeling, centerlines and associated geometric descriptors were extracted using Mimics from cases Normal 1, Normal 7, Diseased 7, and Diseased 9. Thereafter, curvature and tangent vectors were utilized to compute bifurcation angles and curvature values between consecutive segments, as presented in Tables 3.1 and 3.2. Based on the results and insights discussed in Section 4, the approach of segment differentiation by curvature

alone was not pursued further. However, the identification of segments based on bifurcation detection was implemented, as illustrated in Figure 3.8. These results demonstrate that, although the method effectively differentiated bifurcation points, its performance was strongly dependent on the input data order, a limitation further examined in Section 4.

Table 3.1: Bifurcation angles in degrees between adjacent segments. Segment numbers follow the standard in Table 1.1. Missing values indicate bifurcations not present in the case.

Case	3 – 4	3 – 16	4 – 16	5 – 6	5 – 11	6 – 9	7 – 10	11 – 12	13 – 14
Normal 1	68.14	85.42	28.11	50.85	56.69	49.79	35.37	96.81	–
Normal 7	92.18	38.33	129.69	52.50	84.55	100.01	–	66.60	93.44
Diseased 7	88.80	85.09	142.70	49.09	95.70	23.18	93.12	–	–
Diseased 9	107.97	95.42	14.61	33.61	90.17	106.48	21.20	83.94	–

Table 3.2: Curvature values between adjacent segments, expressed in $\text{mm}^{-1} \times 10^{-2}$. Segment numbers follow the standard in Table 1.1.

Case	1 – 2	2 – 3	6 – 7	7 – 8
Normal 1	8.38	12.99	25.01	6.71
Normal 7	4.97	8.62	13.52	5.88
Diseased 7	7.84	13.85	17.05	6.21
Diseased 9	8.21	14.26	18.07	6.54

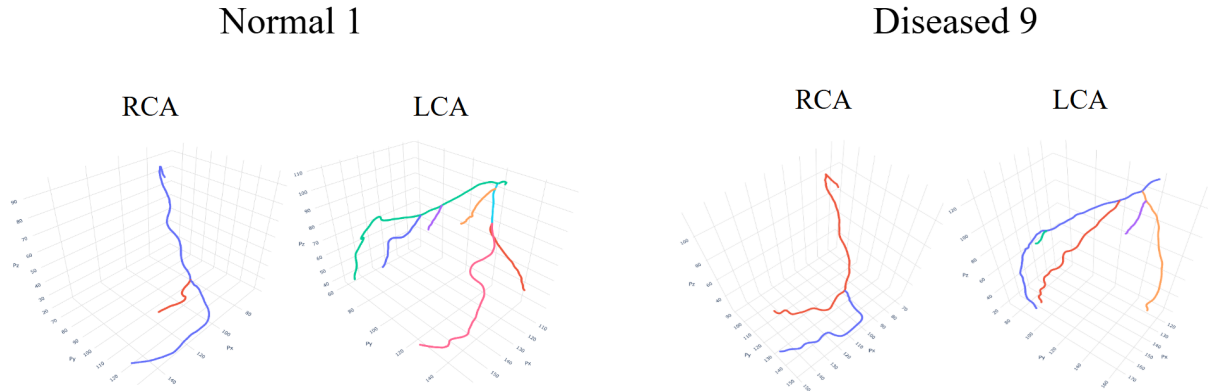


Figure 3.8: Results of bifurcation detection using a 35° angle threshold in the Normal 1 and Diseased 9 ASOCA cases. Colours delineate regions between detected bifurcations and are intended solely for visual distinction. RCA: Right coronary artery. LCA: Left coronary artery.

For the strategy based on heuristic and topological rules, the centerline of the case Normal 1 was also extracted using Mimics and served as the reference example. Once the algorithm produced correct results on this case, as shown in Figure 3.9, the method was further refined. Rather than applying the same approach to additional cases, it was decided to enhance the strategy by incorporating anatomical information from the heart chambers, as described in Section 2.3.3. Consequently, the final version of the heuristic-based method was applied exclusively to the Normal 1 case, and the resulting segmentation output is shown in Figure 3.9, correctly illustrating the anatomical segment labels.

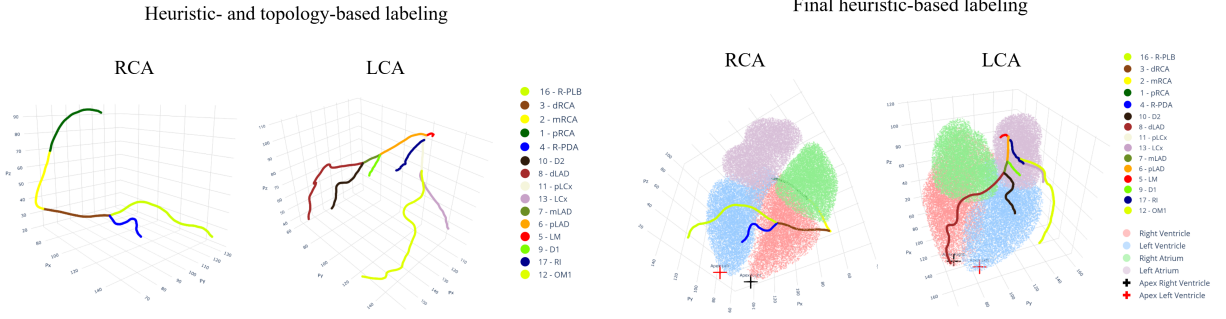


Figure 3.9: Heuristic labeling methods for RCA and LCA segments in ASOCA case Normal 1. Left: Heuristic- and topology-based labeling of RCA and LCA segments. Right: Final heuristic-based labeling of RCA and LCA segments.

3.3 Machine learning-based labeling

For the ML strategy employing solely the coordinates of the centerline points of the coronary arteries as features, a total of 18 ML algorithms (nine tree-based and nine non-tree-based) were trained, considering the RCA and LCA separately. Table 3.3 presents the resulting accuracy for each algorithm. As can be observed, the algorithm that achieved the highest accuracy for the RCA was the SVM, reaching an accuracy of 0.71, whereas the Logistic Regression algorithm performed best for the LCA, attaining an accuracy of 0.44. Examples of the results for these two models are illustrated in Figure 3.10, and their classification reports are shown in Table 3.4 and 3.4.

Table 3.3: Accuracy of ML classifiers for RCA and LCA labeling using coordinate-based features (left) and graph-derived features (right). Tree-based models are shown above the line, non-tree-based models below. Best results in bold.

Model	Coordinate-based		Graph features-based	
	RCA	LCA	RCA	LCA
Random Forest	0.67	0.35	0.92	0.55
Gradient Boosting	0.67	0.36	0.93	0.51
Extra Trees	0.67	0.34	0.92	0.55
XGBoost	0.67	0.34	0.90	0.52
Decision Tree	0.65	0.33	0.89	0.50
AdaBoost	0.56	0.37	0.70	0.47
LightGBM	0.68	0.32	0.91	0.51
CatBoost	0.65	0.34	0.91	0.53
Histogram-based Gradient Boosting	0.68	0.32	0.90	0.52
Logistic Regression	0.70	0.44	0.93	0.57
Perceptron	0.58	0.18	0.83	0.47
Ridge	0.67	0.40	0.83	0.51
SVM	0.71	0.38	0.93	0.50
KNN	0.63	0.32	0.87	0.46
Gaussian Naive Bayes	0.71	0.39	0.88	0.51
LDA	0.68	0.40	0.93	0.56
QDA	0.70	0.44	0.86	0.50
MLP	0.66	0.34	0.92	0.50

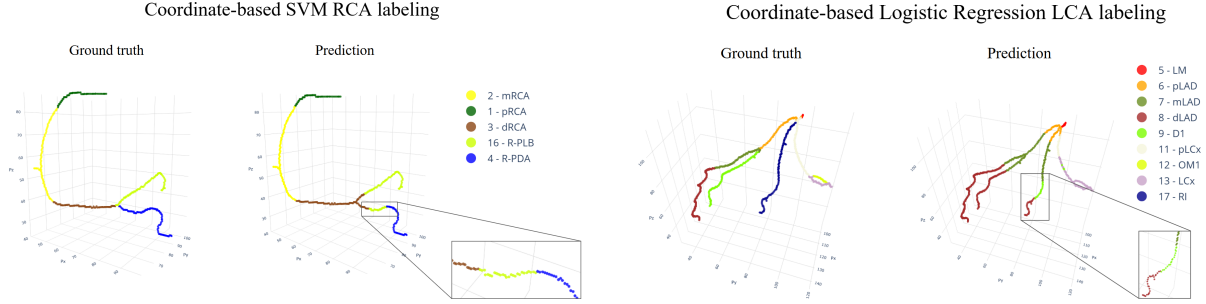


Figure 3.10: Coordinate-based ML labeling for RCA and LCA segments in ASOCA case Normal 16. Left: Predicted versus true labels for the RCA using the SVM model. Right: Predicted versus true labels for the LCA using the Logistic Regression model.

Table 3.4: Classification report for the RCA using the coordinate-based SVM model.

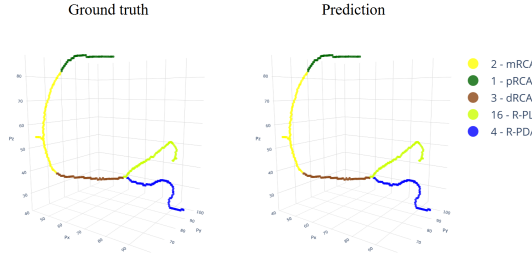
Segment	Precision	Recall	F1-Score	Support
1	0.90	0.73	0.80	750
2	0.73	0.80	0.76	990
3	0.80	0.66	0.72	1028
4	0.67	0.70	0.68	807
16	0.57	0.68	0.62	1037
Accuracy			0.71	4612
Macro Avg	0.73	0.71	0.72	4612
Weighted Avg	0.73	0.71	0.71	4612

Table 3.5: Classification report for the LCA using the coordinate-based Logistic Regression model.

Segment	Precision	Recall	F1-Score	Support
5	0.63	0.66	0.65	402
6	0.31	0.40	0.35	675
7	0.44	0.39	0.41	696
8	0.81	0.74	0.77	1567
9	0.36	0.29	0.32	1015
10	0.14	0.59	0.23	133
11	0.38	0.28	0.32	656
12	0.00	0.00	0.00	461
13	0.41	0.77	0.53	1026
14	0.00	0.00	0.00	189
17	0.00	0.00	0.00	659
Accuracy			0.44	7479
Macro Avg	0.32	0.37	0.33	7479
Weighted Avg	0.41	0.44	0.42	7479

On the other hand, for the ML approach that integrated graph-derived features, the same set of 18 models was trained independently for the RCA and LCA. The resulting accuracies are reported also in Table 3.3. As shown, the algorithm that achieved the highest accuracy for both the RCA and LCA was Logistic Regression, with 0.93 for the RCA and 0.57 for the LCA, thereby improving upon the results obtained from the previous method. Examples of these results are illustrated in Figure 3.11, while the corresponding classification reports are shown in Tables 3.6 and 3.7. Once Logistic Regression was selected as the most suitable model for this task, the feature importance metric was calculated for each feature. The analysis revealed that the most representative feature in both arteries was the node index within the graph (i.e., the order in which the MST organizes the nodes). The feature importance plots are shown in Figures 3.12.

Graph features-based Logistic Regression RCA labeling



Graph features-based Logistic Regression LCA labeling

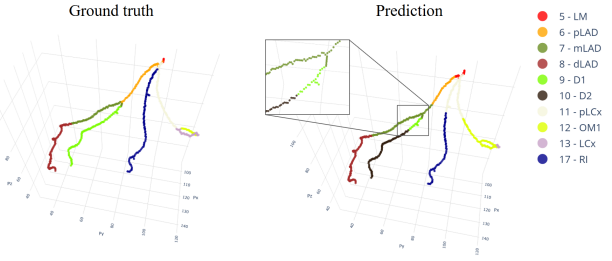


Figure 3.11: Predicted versus true labels for case Normal 16 using the Logistic Regression classifier trained on graph-based features. Left: RCA. Right: LCA.

Table 3.6: Classification report for the RCA using the graph features-based Logistic Regression model.

Segment	Precision	Recall	F1-Score	Support
1	1.00	0.97	0.99	750
2	0.98	0.93	0.95	990
3	0.92	0.80	0.85	1028
4	0.79	0.99	0.88	807
16	1.00	1.00	1.00	1037
Accuracy		0.93	4612	
Macro Avg	0.94	0.94	0.93	4612
Weighted Avg	0.94	0.93	0.93	4612

Table 3.7: Classification report for the LCA using the graph features-based Logistic Regression model.

Segment	Precision	Recall	F1-Score	Support
5	0.72	0.74	0.73	402
6	0.63	0.65	0.64	675
7	0.64	0.56	0.60	696
8	0.93	0.75	0.83	1567
9	0.49	0.38	0.43	1015
10	0.07	0.38	0.12	133
11	0.76	0.63	0.69	656
12	0.25	0.09	0.13	461
13	0.48	0.76	0.59	1026
14	0.00	0.00	0.00	189
17	1.00	0.46	0.63	659
Accuracy		0.57	7479	
Macro Avg	0.54	0.49	0.49	7479
Weighted Avg	0.65	0.57	0.59	7479

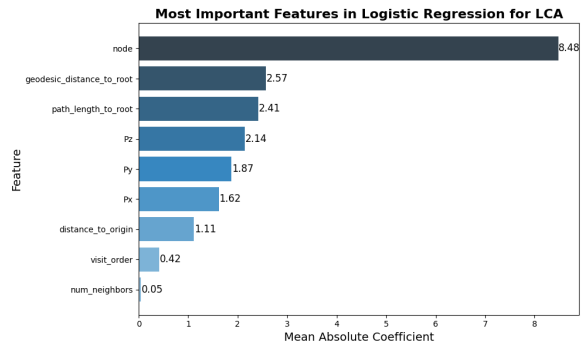
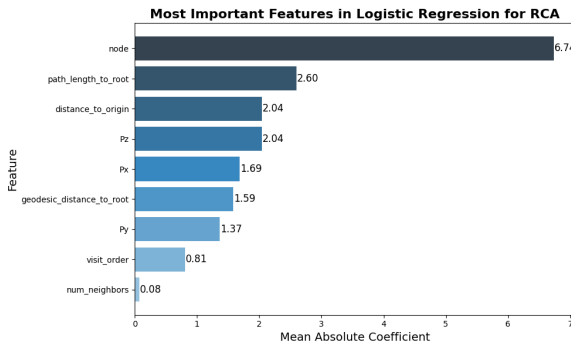


Figure 3.12: Feature importance analysis for RCA and LCA labeling using the Logistic Regression model trained on graph-derived features.

Finally, since the previous approach proved effective when using the features extracted from the MST graph and the Logistic Regression model, these characteristics were then implemented for this final method within the scope of ML, the segment transition detection strategy. Tables 3.8 and 3.9 present the classification reports for the RCA and LCA, respectively. Moreover, Figure 3.13 illustrates two examples of the output of this method. It can be observed that the model predicts all points as belonging to the neutral class (0), despite the reported accuracy being 0.99. This result is further discussed in Section 4.

Table 3.8: Classification report for RCA segment transition detection with Logistic Regression.

Segment	Precision	Recall	F1-Score	Support
0	0.99	1.00	1.00	4583
1	0.00	0.00	0.00	12
2	0.00	0.00	0.00	9
3	0.00	0.00	0.00	8
Accuracy			0.99	4612
Macro Avg	0.25	0.25	0.25	4612
Weighted Avg	0.99	0.99	0.99	4612

Table 3.9: Classification report for LCA segment transition detection with Logistic Regression.

Segment	Precision	Recall	F1-Score	Support
0	0.99	1.00	1.00	7405
1	0.00	0.00	0.00	12
2	0.00	0.00	0.00	12
3	0.00	0.00	0.00	12
4	0.00	0.00	0.00	12
5	0.00	0.00	0.00	11
6	0.00	0.00	0.00	9
7	0.00	0.00	0.00	5
8	0.00	0.00	0.00	1
Accuracy			0.99	7479
Macro Avg	0.11	0.11	0.11	7479
Weighted Avg	0.98	0.99	0.99	7479

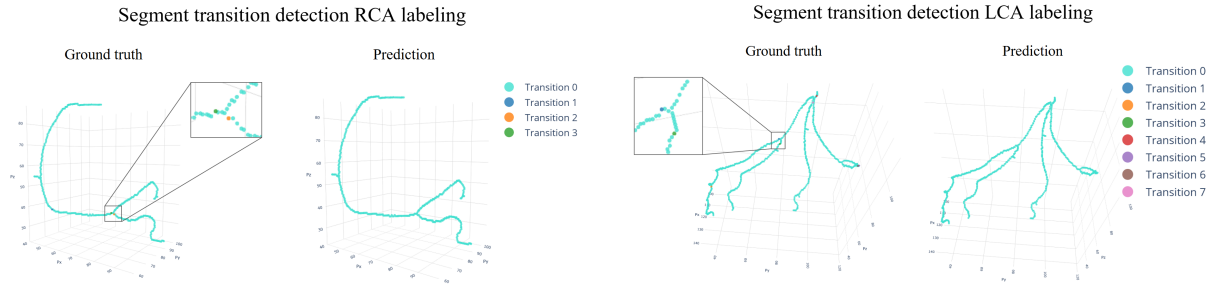


Figure 3.13: Results of segment transition detection using the Logistic Regression model for case Normal 16. Left: RCA. Right: LCA.

3.4 Graph neural network labeling

For the GNN-based strategy, the classification reports corresponding to the right and left coronary arteries are provided in Tables 3.10 and 3.11, respectively. These results yielded moderate overall accuracies of 0.65 for the RCA and 0.43 for the LCA. Moreover, illustrative examples of the labeling outputs generated by both models are presented in Figure 3.14. In these visualizations, clear discontinuities within segments can be observed, suggesting limitations in the model's ability to maintain spatial consistency across anatomically continuous structures.

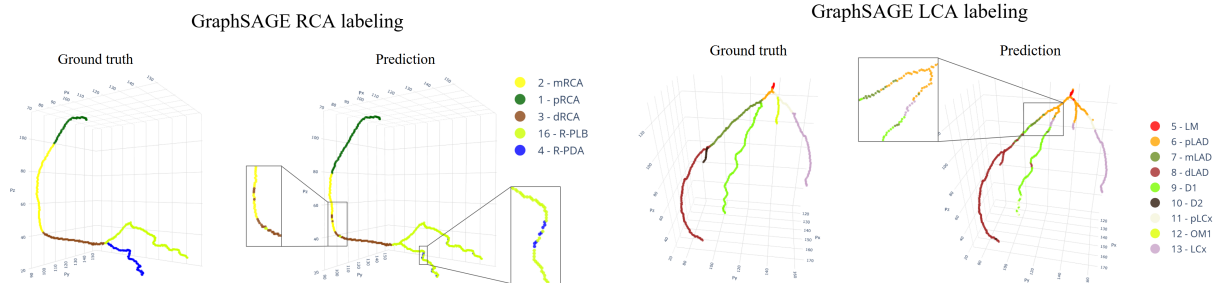


Figure 3.14: GraphSAGE-based labeling for RCA and LCA segments in ASOCA case Diseased 9. Left: Predicted versus true labels for the RCA. Right: Predicted versus true labels for the LCA.

Table 3.10: Classification report for RCA using the GraphSAGE model.

Segment	Precision	Recall	F1-Score	Support
1	0.79	0.97	0.87	488
2	0.93	0.73	0.82	651
3	0.51	0.59	0.55	563
4	0.79	0.24	0.37	681
16	0.50	0.78	0.61	743
Accuracy			0.65	3126
Macro Avg	0.70	0.66	0.64	3126
Weighted Avg	0.70	0.65	0.63	3126

Table 3.11: Classification report for LCA in the case Diseased 9 using the GraphSAGE model.

Segment	Precision	Recall	F1-Score	Support
5	0.57	0.39	0.46	154
6	0.31	0.56	0.40	402
7	0.46	0.44	0.45	488
8	0.53	0.92	0.67	895
9	0.35	0.22	0.27	755
10	0.00	0.00	0.00	195
11	0.39	0.11	0.17	464
12	0.00	0.00	0.00	135
13	0.42	0.97	0.58	719
14	0.23	0.05	0.08	539
17	0.00	0.00	0.00	507
Accuracy			0.43	5253
Macro Avg	0.30	0.33	0.28	5253
Weighted Avg	0.34	0.43	0.34	5253

3.5 Multi-class segmentation labeling

Regarding the coronary segment labeling directly extracted from the CCTA images using the nnU-Net for multi-class segmentation, the results were obtained per fold and per segment. Table 3.12 shows the DSC value for each segment across all folds, as well as the average DSC per segment. Additionally, Table 3.13 presents the average DSC value per fold, highlighting fold 3 as having the maximum score.

Table 3.12: DSC per segment and per fold for the nnU-Net model. The table also includes the average DSC per segment across all folds.

Segment ID	Fold 0	Fold 1	Fold 2	Fold 3	Fold 4	Average DSC
1	0.766	0.898	0.794	0.855	0.801	0.823
2	0.733	0.833	0.794	0.794	0.651	0.761
3	0.740	0.624	0.802	0.774	0.619	0.712
4	0.375	0.000	0.000	0.465	0.000	0.168
5	0.802	0.848	0.831	0.741	0.830	0.811
6	0.799	0.846	0.809	0.668	0.777	0.780
7	0.673	0.636	0.469	0.526	0.541	0.569
8	0.689	0.000	0.586	0.652	0.000	0.385
9	0.358	0.000	0.000	0.222	0.000	0.116
10	0.085	0.000	0.000	0.192	0.000	0.055
11	0.723	0.783	0.749	0.577	0.488	0.664
12	0.108	0.000	0.000	0.087	0.000	0.039
13	0.383	0.585	0.503	0.502	0.459	0.486
14	0.076	0.000	0.000	0.063	0.000	0.028
15	–	–	–	–	–	–
16	0.426	0.000	0.000	0.453	0.000	0.176
17	0.000	0.000	0.000	0.235	0.000	0.047
18	–	–	–	–	–	–
19	0.229	0.000	0.000	0.266	0.000	0.099

Table 3.13: Average DSC obtained by the nnU-Net model across the five cross-validation folds. The highest score is highlighted in bold.

Fold	Average DSC
Fold 0	0.468
Fold 1	0.356
Fold 2	0.373
Fold 3	0.475
Fold 4	0.304

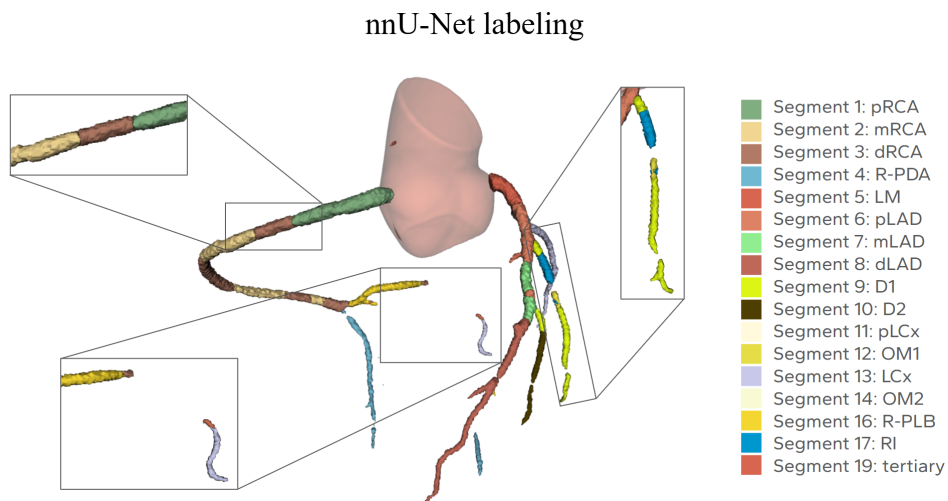


Figure 3.15: Example of the nnU-Net multi-class segmentation result, with defects highlighted (case Diseased 18).

Chapter 4

DISCUSSION

4.1 Interpretation of the results

The initial strategy based on curvature and bifurcation angles was inspired by clinical observations, as cardiologists at Hospital de Sant Pau highlighted these anatomical features as key indicators for distinguishing segments. However, as presented in Table 3.1 and Table 3.2, bifurcation angles and curvature values varied significantly across cases, with bifurcation angles ranging from 14.6° to 142.7° , and curvature values between 0.05 mm^{-1} and 0.25 mm^{-1} . This inconsistency indicated that a fixed threshold would not generalize well, even if the analysis was limited to four cases. Furthermore, the method depended on the ordered output from Mimics, which introduced a structural limitation by assuming a consistent data order. Although Figure 3.8 shows that bifurcation detection was successful, the method failed to differentiate downstream branches as separate segments, typically labeling only one continuation rather than the two anatomically distinct branches. Given these limitations, this method was abandoned.

To overcome these initial shortcomings, the heuristic and topological rule-based method was developed, which successfully labeled the case Normal 1 case without errors, as displayed in Figure 3.9. However, this method relied on idealized centerline extraction and made strong assumptions about the heart's orientation in 3D space. To improve robustness, the final heuristic strategy incorporated anatomical distances to cardiac chambers, reducing dependency on heart orientation and introducing a more meaningful spatial reference system. As depicted in Figure 3.9, this approach produced more anatomically coherent results that aligned more with clinical expectations. Nevertheless, it still presented several limitations, which are explained in the following section.

Transitioning to ML-based methods, the coordinate-based approach achieved modest performance, with the best results obtained using an SVM for the RCA (0.71 accuracy) and Logistic Regression for the LCA (0.44 accuracy), as presented in Table 3.3. Despite the initial hypothesis that tree-based models would perform better due to the tree-like structure of coronary arteries, the results did not support this assumption. The classification reports and Figure 3.10 reveal that models relying solely on spatial coordinates (P_x, P_y, P_z) struggled to capture the topological complexity of the coronary tree. Predictions were primarily based on sample positions, leading to discontinuities where labels changed abruptly within the same segment. In the RCA (Table 3.4), more frequent segments, such as 1 (pRCA) and 2 (mRCA), achieved F1-scores greater than 0.75. In contrast, smaller or less frequent segments, such as 16 (R-PLB), exhibited lower

values. The LCA results further emphasised this limitation, with several segments, including 12 (OM1), 14 (OM2), and 17 (RI), remaining unlabeled (Table 3.5). These findings, demonstrate that spatial coordinates alone are insufficient for reliable segment labeling and highlight the need to incorporate anatomical features and structural information to achieve robust and clinically meaningful results.

To address these deficiencies, the graph features-based ML approach incorporated topological information derived from the MST. This addition notably increased the accuracy, reaching 0.93 for RCA and 0.57 for LCA, as presented in Table 3.3. The feature importance analysis provided in Figure 3.12 reported that the node index was the most influential feature (6.74 for RCA, 8.48 for LCA). Features related to branching, such as the number of neighbors and visit order, had negligible importance, suggesting the model primarily relied on sequential position rather than exploiting branching complexity. The RCA classification report (Table 3.6) showed excellent results, with F1-scores above 0.85 for all segments and perfect predictions in the example provided in Figure 3.11. For the LCA, however, accuracy remained limited, with poor performance in segments such as 12 (OM1) and 14 (OM2), as detailed in Table 3.7. Nonetheless, the model preserved label consistency within branches, reducing abrupt changes and improving anatomical plausibility compared to coordinate-only models. These results highlight the value of topological features, yet also emphasize limitations in modeling anatomical variability, particularly in the LCA.

In an attempt to simplify the problem, a model was trained to detect only segment transitions rather than full classifications. This strategy was implemented using the Logistic Regression model with the same graph features as the previous method. This choice was motivated by the strong performance of the ML model in the graph features-based classification task, where it achieved the highest accuracy for both RCA and LCA. However, the results revealed critical limitations. Although the overall accuracy appeared high, the model failed to identify any transition points. As presented in Tables 3.8 and 3.9, almost all points were classified as class 0 (non-transition), and F1-score, recall and precision for the transition classes were zero. This result can be attributed to the substantial imbalance between transition and non-transition points in the dataset, which led the model to prioritize the prediction of the majority class while disregarding the minority classes. The example outputs in Figure 3.13 confirm that no transition points were detected correctly. Although the idea of detecting only segment changes is conceptually promising, this formulation proved ineffective.

Given the tree-like nature of coronary arteries, GraphSAGE was explored as a method capable of directly modeling the data as a graph structure. The rationale behind this choice was to leverage the connectivity information between points, which previous methods had struggled to fully capture. However, the results demonstrated important limitations. The GraphSAGE models achieved only moderate accuracy, with a value of 0.65 for the RCA and 0.43 for the LCA, as reported in Tables 3.10 and 3.11. The visualizations presented in Figure 3.14 further supported these findings. Label continuity was not preserved within branches, and points within the same anatomical segment were inconsistently labeled, leading to fragmented predictions. Furthermore, training dynamics revealed early saturation: test loss fluctuated and test accuracy stagnated after initial improvement, indicating limited learning capacity and the need for architectural or feature enhancements. Due to time constraints, further refinement of the architecture and the incorporation of enhanced node features could not be implemented.

Given the limitations of centerline-based methods, a different approach was explored using

nnU-Net to directly segment coronary arteries from CCTA images. This strategy aligned with state-of-the-art methods for medical image segmentation, aiming to learn voxel-level patterns from the data. However, the results revealed significant challenges. The average DSC across folds were modest, ranging from 0.30 to 0.47, as reported in Table 3.13. Moreover, the per-segment DSC exhibited considerable variability. Proximal segments such as segment 1 (pRCA), and segment 5 (LM) achieved relatively high scores, typically above 0.80, while smaller or peripheral branches like segments 10 (D2), 12 (OM1), 14 (OM2), 17 (RI) and 19 presented DSC values below 0.06, with several folds yielding values of zero, as indicated in Table 3.12. This pattern indicates that the model, when presented with segments that are infrequent or occupy a very small volume, often chose not to predict them at all. By doing so, the model avoided false positives but completely missed the true positives, leading to the omission of these minor or peripheral branches in the segmentation results. In addition, the segmentation outputs, as illustrated in Figure 3.15, were fragmented, exhibiting disconnected structures and discontinuities across segments. These results underline a fundamental limitation: the nnU-Net architecture does not account for anatomical context or branch connectivity.

Ultimately, these results should be interpreted in the context of recent advances in automatic coronary segment labeling. While state-of-the-art methods such as TopoLab, Neural Syntax Parser, CPR-GCN, TreeLab-Net, and CorLab-Net report mean F1-scores between 0.87 and 0.96 on large and diverse datasets, the heuristic and classical machine learning strategies developed in this thesis achieved only moderate performance, especially when based solely on geometric or coordinate features. The integration of graph-derived features led to some improvement for the RCA, but overall, none of the proposed approaches reached the accuracy and robustness of advanced models introduced in Section 1. In addition, the nnU-Net multi-class segmentation obtained better results in proximal segments but struggled in more distal or complex branches, as has also been reported in the literature. Altogether, these findings highlight that methods which fully exploit anatomical topology, spatial context, and large-scale data remain the most effective for achieving clinically reliable coronary segment labeling.

4.2 Challenges and limitations

This study faced several challenges and limitations, both in terms of data and methodology. The most significant constraint stemmed from the dataset itself: the ASOCA dataset, while publicly available and widely used in the community, was limited in size, comprising only 40 cases, all of which exhibited right coronary dominance. The absence of left-dominant cases and the underrepresentation or complete absence of specific segments, such as the L-PDA and L-PLB, severely limited the model's capacity to generalize across the full anatomical spectrum. Furthermore, the ASOCA segmentations were incomplete, often lacking tertiary branches and exhibiting structural inconsistencies due to motion artifacts or low image quality. Likewise, in most cases, segments were already present, but their length was not correct, leading to discrepancies in anatomical continuity. These deficiencies affected the reliability of the generated ground truth and subsequently hindered model performance across all approaches. Additionally, the decision to exclude tertiary branches from the initial experiments, although a pragmatic choice for stepwise complexity escalation, also introduced a structural bias. This simplification, combined with occasional irregularities in the extracted centerlines due to the use of unsmoothed segmented structure, reduced the anatomical fidelity of the data and limited the representative-

ness of the cases, particularly for modeling complex bifurcation patterns or rare anatomical variants.

From a methodological standpoint, firstly, the curvature and bifurcation-based method presented limited robustness and generalizability, as variability across cases made consistent thresholds unfeasible. Moreover, its reliance on proprietary software like Mimics limited reproducibility and accessibility. Open-source alternatives would be preferable to support broader adoption and clinical integration. Thereafter, in order to address these limitations inherent in detecting bifurcations, the coronary arteries were subsequently modeled as a graph structure using the MST algorithm. This graph-based approach enabled the encoding of both spatial and topological relationships, providing greater robustness to anatomical variability. This approach facilitated the identification of bifurcation points and improved the structural consistency of the labeling process. Building upon this framework, the final heuristic algorithm incorporated distances to cardiac chambers, which improved anatomical plausibility compared to earlier rule-based methods. However, it remained limited by its reliance on distance metrics alone, which may not capture the full complexity of coronary anatomy. The exclusion of tertiary branches and the use of simplified centerline extraction further constrained its applicability. In addition, the method was only validated on a single case, limiting its ability to generalize to anatomically diverse or clinically complex scenarios.

Regarding ML methods, a key limitation was their treatment of each point in isolation, relying solely on absolute 3D coordinates. This approach disregarded the anatomical connectivity of the coronary tree, leading to fragmented predictions and failure to capture spatial continuity. Although the graph features-based method introduced structural information, it still lacked a full representation of inter-point dependencies. This was especially limiting in the LCA, where anatomical variability is higher and segment transitions are more complex. On the other hand, the segment transition detection method was severely impacted by class imbalance, as transition points were underrepresented. Consequently, the model defaulted to predicting the most present class, which corresponded to points without transitions, achieving high apparent accuracy but failing to detect any actual transitions.

Similarly, the GNN approach showed clear limitations that affected its performance. The Graph-SAGE model was implemented with only two convolutional layers and relied solely on spatial coordinates as node features, limiting its ability to capture complex anatomical relationships. It did not incorporate crucial information such as vessel diameter, curvature, or bifurcation context. Additionally, the small and homogeneous dataset restricted the model's capacity to learn representations that could generalize to anatomically diverse cases.

Finally, the nnU-Net experiments revealed key limitations in segmenting coronary artery segments directly from CCTA images. The architecture does not incorporate anatomical context or branch connectivity, which resulted in fragmented and anatomically inconsistent outputs. DSC values remained modest and performance was particularly poor for smaller or less frequent segments. Furthermore, the outputs included disconnected structures and lacked continuity across segments. These findings emphasise the need for methods that explicitly model anatomical structure to achieve coherent and clinically useful segmentations.

4.3 Potential improvements and future lines of research

Given the limited and anatomically biased dataset used in this study, future work should focus on expanding the data. A promising direction would be to re-label the coronary segments in the ImageCAS dataset [44], which contains CCTA images with their respective segmentations from 1,000 patients. It should be noted, however, that the segmentation quality and completeness in ImageCAS are not superior to those of ASOCA, as some segmentations remain incomplete and may require additional refinement. Nevertheless, this dataset would provide a more diverse and representative ground truth, including left-dominant anatomies and rare variants, and enable the training of more generalizable models for automatic coronary segment labeling.

Likewise, re-segmenting the original ASOCA cases could significantly enhance data completeness and improve the quality of the ground truth annotations. This initiative, currently in progress at Hospital de Sant Pau, is expected to make a substantial contribution to the anatomical consistency of the dataset. In parallel, applying smoothing algorithms to the segmentations before extracting the centerlines could help reduce irregularities and produce more anatomically accurate vessel trajectories.

From a methodological perspective, hybrid models that combine heuristics and ML present a promising avenue. For instance, segments could be pre-labeled using ML models and then refined using heuristic rules informed by clinical knowledge, ensuring anatomical coherence and improving label consistency across the coronary tree. Furthermore, enhancing ML approaches with richer features such as vessel diameter, curvature or branching angles would allow models to better capture the structural complexity of coronary anatomy.

In addition, GNNs remain one of the most promising directions for future research. Although the GraphSAGE model explored in this study showed modest results, its ability to directly model connectivity and spatial dependencies suggests considerable potential for anatomical labeling tasks. Future efforts should focus on exploring a broader range of GNN architectures and on fine-tuning their hyperparameters for anatomical data. Incorporating richer node features, including curvature, vessel radius, or flow orientation, could enhance the GNN’s ability to capture anatomical complexity. Furthermore, increasing the number of graph convolutional layers and introducing regularization techniques such as dropout or batch normalization may alleviate overfitting and improve generalization.

On the other hand, refining evaluation metrics to account for clinical relevance would represent a meaningful advancement. In practice, mislabeling a primary segment carries more severe implications than errors in distal branches. Future research should explore clinically weighted evaluation frameworks that assign greater penalties to misclassifications in primary segments. Such an approach would better align model assessment with clinical priorities and diagnostic impact.

Lastly, the integration of clinical validation by expert cardiologists is essential not only during the creation of the ground truth but also throughout the evaluation of automated labeling results. Future studies should incorporate error analyses in close collaboration with heart specialist, and evaluate the system’s potential to reduce diagnostic time and support clinical decision-making. Such comprehensive validation is crucial to ensure that the automated labeling approaches are reliable, clinically meaningful, and suitable for practical implementation in real-world settings.

Chapter 5

CONCLUSION

This bachelor's thesis has presented a comprehensive analysis and development of multiple strategies for the automatic anatomical labeling of coronary artery segments, addressing a crucial step in the diagnosis of CAD. Through a multi-strategy approach, the work explored and evaluated a diverse set of methodologies ranging from geometry-based heuristics to advanced deep learning models. These included bifurcation and curvature-driven heuristics, rule-based systems enhanced with anatomical context, classical ML classifiers, neural network graph-based learning strategies, and a fully automated nnU-Net segmentation framework.

The project was grounded on a clinically guided dataset created from the ASOCA challenge, enriched through manual annotation and expert validation at Hospital de Sant Pau. The dataset served as a fundamental resource for developing and testing the proposed approaches, despite its inherent limitations such as anatomical incompleteness and right dominance bias.

The results have demonstrated the strengths and weaknesses of each methodology. Geometric heuristics-based strategies offered limited robustness due to their sensitivity to noise and anatomical variability. In contrast, the topological rule-based methods—particularly when incorporating anatomical distances to heart chambers—achieved accurate labeling in selected cases, offering strong interpretability and clinical consistency. ML models using graph-derived features yielded the highest classification performance, especially with Logistic Regression, highlighting the importance of incorporating structural information. Meanwhile, the direct multi-class segmentation approach provided promising results in large vessels but struggled with distal branches and coronary artery topology.

Collectively, the findings highlight the value of combining anatomical knowledge, graph representations, and learning-based models to advance coronary artery labeling. While no single method proved universally optimal, their complementarity provides key insights for the design of future hybrid systems. This thesis lays a solid groundwork for future research and clinical integration, offering practical tools and methodological foundations to support more efficient and accurate CAD diagnosis. Further work should focus on validating the proposed methods on larger, more diverse datasets, integrating them into clinical workflows, and combining rule-based and deep learning strategies to enhance robustness and scalability.

Bibliography

- [1] Servier Medical Art. *Drawing Coronary arteries and veins - no labels*. Licensed under Creative Commons Attribution (CC BY). n.d. URL: <https://anatomytool.org/content/servier-drawing-coronary-arteries-and-veins-no-labels> (visited on 05/24/2025).
- [2] Cleveland Clinic. *Coronary Arteries: Anatomy and Function*. 2022. URL: <https://my.clevelandclinic.org/health/body/22973-coronary-arteries>.
- [3] Mayo Clinic. *Coronary Artery Disease - Symptoms and Causes*. 2024. URL: <https://www.mayoclinic.org/diseases-conditions/coronary-artery-disease/symptoms-causes/syc-20350613>.
- [4] Kaiser Permanente. *Cardiology – Coronary artery disease – Image – TPMG*. Accessed May 2025. 2025. URL: <https://mydoctor.kaiserpermanente.org>.
- [5] Cleveland Clinic. *Coronary Artery Disease*. 2023. URL: <https://my.clevelandclinic.org/health/diseases/16898-coronary-artery-disease>.
- [6] World Health Organization. *The Top 10 Causes of Death*. 2024. URL: <https://www.who.int/news-room/fact-sheets/detail/the-top-10-causes-of-death>.
- [7] European Society of Cardiology. *ESC Cardiovascular Realities* 2024. Based on data from the ESC Atlas of Cardiology 2023. Accessed: 2025-06-08. 2024. URL: <https://www.escardio.org/Research/ESC-Atlas-of-Cardiology>.
- [8] Instituto Nacional de Estadística (INE). *Estadísticas sobre enfermedades del corazón*. 2024. URL: <https://www.ine.es/dynt3/inebase/es/index.htm?padre=4858>.
- [9] J Leipsic et al. “SCCT guidelines for the interpretation and reporting of coronary CT angiography: a report of the Society of Cardiovascular Computed Tomography Guidelines Committee”. In: *Journal of Cardiovascular Computed Tomography* 8.5 (2014), pp. 342–358. DOI: [10.1016/j.jcct.2014.07.003](https://doi.org/10.1016/j.jcct.2014.07.003).
- [10] Manuel D. Cerqueira et al. “Standardized myocardial segmentation and nomenclature for tomographic imaging of the heart: A statement for healthcare professionals from the cardiac imaging committee of the council on clinical cardiology of the American Heart Association”. In: *Circulation* 105.4 (2002), pp. 539–542. DOI: [10.1161/01.CIR.0402.102975](https://doi.org/10.1161/01.CIR.0402.102975).
- [11] James S. Shahoud, Manoj Ambalavanan, and Vijai S. Tivakaran. *Cardiac Dominance*. StatPearls [Internet]. Bethesda (MD): National Library of Medicine (US); 2022 Sep 26. 2022. URL: <https://www.ncbi.nlm.nih.gov/books/NBK537207/>.

- [12] ASOCA Challenge: Automatic Segmentation of Coronary Arteries. <https://asoca.grand-challenge.org/>.
- [13] Siemens Healthineers. Syngo.Via - Molecular Imaging Software for PET-CT. 2024. URL: <https://www.siemens-healthineers.com/en-us/molecular-imaging/pet-ct/syngo-via>.
- [14] Zhixing Zhang et al. “Topology-Preserving Automatic Labeling of Coronary Arteries via Anatomy-Aware Connection Classifier”. In: *Medical Image Computing and Computer-Assisted Intervention – MICCAI 2023*. Vol. 14226. Lecture Notes in Computer Science. 2023, pp. 759–769. DOI: [10.1007/978-3-031-43990-2_71](https://doi.org/10.1007/978-3-031-43990-2_71).
- [15] Ashish Vaswani et al. “Attention is all you need”. In: *Advances in Neural Information Processing Systems*. Vol. 30. Curran Associates, Inc., 2017, pp. 5998–6008. URL: <https://doi.org/10.48550/arXiv.1706.03762>.
- [16] C. Zhou and L. Hu. “A Neural Syntax Parser for Coronary Artery Anatomical Labeling in Coronary CT Angiography”. In: *ICASSP 2024 - 2024 IEEE International Conference on Acoustics, Speech and Signal Processing (ICASSP)*. Seoul, Korea, Republic of, 2024, pp. 2051–2055. DOI: [10.1109/ICASSP48485.2024.10448334](https://doi.org/10.1109/ICASSP48485.2024.10448334).
- [17] H. Yang et al. “CPR-GCN: Conditional Partial-Residual Graph Convolutional Network in Automated Anatomical Labeling of Coronary Arteries”. In: *2020 IEEE/CVF Conference on Computer Vision and Pattern Recognition (CVPR)*. Seattle, WA, USA, 2020, pp. 3802–3810. DOI: [10.1109/CVPR42600.2020.00386](https://doi.org/10.1109/CVPR42600.2020.00386).
- [18] D. Wu et al. “Automated anatomical labeling of coronary arteries via bidirectional tree LSTMs”. In: *International Journal of Computer Assisted Radiology and Surgery* 14.2 (2019), pp. 271–280. DOI: [10.1007/s11548-018-1884-6](https://doi.org/10.1007/s11548-018-1884-6).
- [19] X. Zhang et al. “CorLab-Net: Anatomical Dependency-Aware Point-Cloud Learning for Automatic Labeling of Coronary Arteries”. In: *Machine Learning in Medical Imaging. MLMI 2021*. Ed. by C. Lian et al. Vol. 12966. Lecture Notes in Computer Science. Springer, Cham, 2021, pp. 576–585. DOI: [10.1007/978-3-030-87589-3_59](https://doi.org/10.1007/978-3-030-87589-3_59).
- [20] G. Yang et al. “Automatic Coronary Artery Tree Labeling in Coronary Computed Tomographic Angiography Datasets”. In: *Computing in Cardiology*. Vol. 38. IEEE. Hangzhou, China, 2011, pp. 109–112. URL: <https://www.cinc.org/archives/2011/pdf/0109.pdf>.
- [21] Pengling Ren et al. “A deep learning-based automated algorithm for labeling coronary arteries in computed tomography angiography images”. In: *BMC Medical Informatics and Decision Making* 23.249 (2023). DOI: [10.1186/s12911-023-02332-y](https://doi.org/10.1186/s12911-023-02332-y). URL: <https://doi.org/10.1186/s12911-023-02332-y>.
- [22] R. Shahzad et al. “Automatic segmentation, detection and quantification of coronary artery stenoses on CTA”. In: *International Journal of Cardiovascular Imaging* 29.8 (2013), pp. 1847–1859. DOI: [10.1007/s10554-013-0271-1](https://doi.org/10.1007/s10554-013-0271-1).
- [23] Özgün Çiçek et al. *3D U-Net: Learning Dense Volumetric Segmentation from Sparse Annotation*. Preprint. arXiv:1606.06650. 2016. arXiv: [1606.06650 \[cs.CV\]](https://arxiv.org/abs/1606.06650). URL: <https://doi.org/10.48550/arXiv.1606.06650>.
- [24] C. Acebes Pinilla. *An Artificial Intelligence Framework for the Prioritization and Reporting of Coronary Artery Disease Patients in a Radiology Department*. Sept. 2023.

- [25] A. P. Carnicelli et al. “Cross-sectional area for the calculation of carotid artery stenosis on computed tomographic angiography”. In: *Journal of Vascular Surgery* 58.3 (2013), pp. 659–665. DOI: [10.1016/j.jvs.2013.02.031](https://doi.org/10.1016/j.jvs.2013.02.031).
- [26] Eva Ferrer Beltran. “Enhanced prioritization and reporting for coronary artery disease diagnosis”. Bachelor’s thesis. Universitat Pompeu Fabra, 2024.
- [27] Cesar Acebes et al. “The Centerline-Cross Entropy Loss for Vessel-Like Structure Segmentation: Better Topology Consistency Without Sacrificing Accuracy”. In: *Medical Image Computing and Computer Assisted Intervention – MICCAI 2024*. Ed. by Marius George Linguraru et al. Vol. 15008. Lecture Notes in Computer Science. Cham: Springer Nature Switzerland, 2024, pp. 710–720. ISBN: 978-3-031-72111-3. DOI: [10.1007/978-3-031-72111-3_67](https://doi.org/10.1007/978-3-031-72111-3_67). URL: https://doi.org/10.1007/978-3-031-72111-3_67.
- [28] R. Gharleghi et al. “Automated segmentation of normal and diseased coronary arteries – The ASOCA challenge”. In: *Computerized Medical Imaging and Graphics* 97 (Apr. 2022), p. 102049. DOI: [10.1016/j.compmedimag.2022.102049](https://doi.org/10.1016/j.compmedimag.2022.102049).
- [29] A. Fedorov et al. *3D Slicer: A Platform for Subject-Specific Image Analysis, Visualization, and Clinical Support*. <https://www.slicer.org/>. Accessed: 2025-03-08. 2012.
- [30] NiBabel developers. *NiBabel (version 5.3.2) [software]*. <https://pypi.org/project/nibabel/>. Accessed: 2025-05-18. 2024.
- [31] Stéfan van der Walt et al. “scikit-image: Image processing in Python”. In: *PeerJ* 2 (2014), e453. DOI: [10.7717/peerj.453](https://doi.org/10.7717/peerj.453). URL: <https://doi.org/10.7717/peerj.453>.
- [32] Luis Ibáñez et al. *The ITK Software Guide*. Clifton Park, NY, USA: Kitware, Inc., 2005.
- [33] Bradley C Lowe kamp et al. “Design of a Simplified Interface for the Insight Toolkit”. In: *Frontiers in Neuroinformatics* 7 (2013), p. 45. DOI: [10.3389/fninf.2013.00045](https://doi.org/10.3389/fninf.2013.00045).
- [34] Aric A. Hagberg, Daniel A. Schult, and Pieter J. Swart. *NetworkX*. <https://networkx.org>. Version 3.2.1. Accessed: 2025-05-27. 2008.
- [35] Jakob Wasserthal et al. “TotalSegmentator: Robust segmentation of 104 anatomical structures in CT images”. In: *Nature Communications* 14.1 (2023), p. 10. DOI: [10.1038/s41467-023-36556-5](https://doi.org/10.1038/s41467-023-36556-5). URL: <https://doi.org/10.1038/s41467-023-36556-5>.
- [36] F. Pedregosa et al. “Scikit-learn: Machine Learning in Python”. In: *Journal of Machine Learning Research* 12 (2011), pp. 2825–2830.
- [37] Tianqi Chen and Carlos Guestrin. “XGBoost: A scalable tree boosting system”. In: *Proceedings of the 22nd ACM SIGKDD International Conference on Knowledge Discovery and Data Mining*. ACM. 2016, pp. 785–794.
- [38] Guolin Ke et al. “LightGBM: A Highly Efficient Gradient Boosting Decision Tree”. In: *Advances in Neural Information Processing Systems*. 2017, pp. 3146–3154.
- [39] Liudmila Prokhorenkova et al. “CatBoost: unbiased boosting with categorical features”. In: *Advances in Neural Information Processing Systems*. Vol. 31. 2018, pp. 6638–6648.

- [40] William L. Hamilton, Rex Ying, and Jure Leskovec. “Inductive Representation Learning on Large Graphs”. In: *Proceedings of the 31st International Conference on Neural Information Processing Systems*. Curran Associates Inc., 2017, pp. 1025–1035. URL: <https://proceedings.neurips.cc/paper/2017/file/5dd9db5e033da9c6fb5ba83c7a7e7.pdf>.
- [41] Matthias Fey and Jan E. Lenssen. “Fast Graph Representation Learning with PyTorch Geometric”. In: *arXiv preprint arXiv:1903.02428* (2019). URL: <https://arxiv.org/abs/1903.02428>.
- [42] Fabian Isensee et al. “nnU-Net: a self-configuring method for deep learning-based biomedical image segmentation”. In: *Nature Methods* 18 (2021), pp. 203–211. DOI: [10.1038/s41592-020-01008-z](https://doi.org/10.1038/s41592-020-01008-z). URL: <https://doi.org/10.1038/s41592-020-01008-z>.
- [43] Consorci de Serveis Universitaris de Catalunya (CSUC). *Pirineus III Supercomputer*. <https://www.csuc.cat/en/services/supercomputacio/pirineus>. Accessed June 2025. 2024.
- [44] A. Zeng et al. *ImageCAS: A large-scale dataset and benchmark for coronary artery segmentation based on computed tomography angiography images*. 2023. arXiv: [2211.01607 \[eess.IV\]](https://arxiv.org/abs/2211.01607).
- [45] Guillem Pons-Lladó and Rubén Leta-Petracca, eds. *Atlas of Non-Invasive Coronary Angiography by Multidetector Computed Tomography*. Vol. 259. Developments in Cardiovascular Medicine. New York, NY: Springer, 2006. ISBN: 978-0-387-33044-0. DOI: [10.1007/978-0-387-33048-8](https://doi.org/10.1007/978-0-387-33048-8). URL: <https://doi.org/10.1007/978-0-387-33048-8>.

Appendix A

CORONARY SEGMENT GUIDELINES

The following definitions of the 18 coronary artery segments, which have served as anatomical references throughout this work, are based on clinical guidelines established by the Society of Cardiovascular Computed Tomography (SCCT) [9], and are further refined according to the anatomical criteria and expert guidance of Dr. Rubén Leta Petracca (Cardiac Imaging Unit, Hospital de la Santa Creu i Sant Pau, Barcelona). These definitions closely follow the anatomical descriptions and segmental delineations presented in the book *Atlas of Non-Invasive Coronary Angiography by Multidetector Computed Tomography* [45], co-edited by Dr. Leta Petracca.

A.1 Right coronary artery

To define the proximal, medial and distal segments of the RCA, its natural C-shape curvature is used as a reference. The artery is divided into three segments based on changes in curvature:

- **1: Proximal segment of the RCA (pRCA)**

Extends from the origin of the RCA to the first noticeable curvature. Shown in A.1.

- **2: Medial segment of the RCA (mRCA)**

Extends from the end of the p-RCA to the acute margin of the heart, where the artery bends inferiorly along the atrioventricular groove. The curvature here becomes more pronounced. Shown in A.1.

- **3: Distal segment of the RCA (dRCA)**

Extends from the end of the m-RCA to the origin of the bifurcation into the right posterior descending artery (R-PDA) and right posterolateral branch (R-PLB). Shown in A.2.

- **4: Right posterior descending artery (R-PDA)**

Originates at the end of the d-RCA and follows the inferior interventricular sulcus toward the apex. Shown in A.2 and A.3. In approximately 30% of cases, the PDA is duplicated, as illustrated in A.4.

- **16: Right posterolateral branch (R-PLB)**

Projects toward the posterolateral walls of the left ventricle. Typically, it arises as a terminal branch of the RCA in right-dominant circulation, alongside the R-PDA. Less

frequently, it may arise from the left circumflex artery (LCx) or even the LAD. Shown in A.2 and A.3.

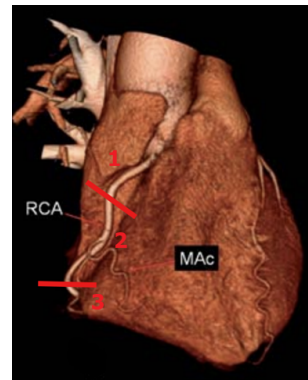


Figure A.1: Example illustrating the division of the first three segments of the RCA: 1 (pRCA), 2 (mRCA), and 3 (dRCA), based on changes in vessel curvature, highlighted in red. MAC: Marginal acute branch. Adapted from Pons-Lladó and Leta-Petracca (2006) [45].

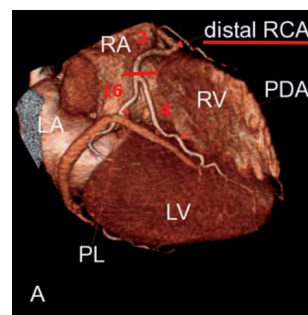


Figure A.2: Example illustrating the division of the last three segments of the RCA: 3 (dRCA), 4 (R-PDA), and 16 (R-PLB), based on bifurcation, highlighted in red. RA: right atrium, LA: left atrium, RV: right ventricle, LV: left ventricle. Adapted from Pons-Lladó and Leta-Petracca (2006) [45].

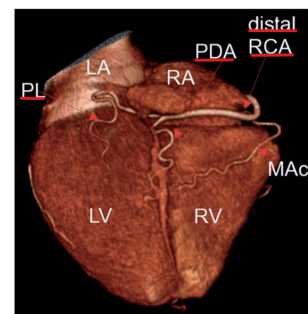


Figure A.3: Example illustrating the last three segments of the RCA: 3 (dRCA), 4 (R-PDA), and 16 (R-PLB), highlighted in red. RA: right atrium, LA: left atrium, RV: right ventricle, LV: left ventricle, MAC: Marginal acute branch. Adapted from Pons-Lladó and Leta-Petracca (2006) [45].

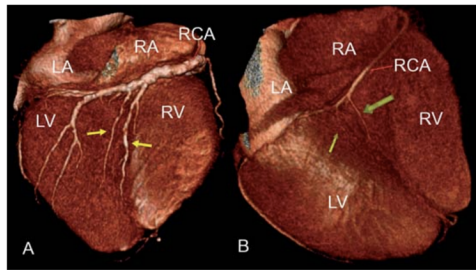


Figure A.4: Examples of posterior descending arteries (PDA): sometimes not a single vessel, but consisting of two or more branches (arrows) of large (A) or small (B) diameter, arising from the distal right coronary artery (dRCA). RA: right atrium, LA: left atrium, RV: right ventricle, LV: left ventricle. From Pons-Lladó and Leta-Petracca (2006) [45].

A.2 Left coronary artery

The LCA originates from the left aortic sinus just above the aortic valve. In 30% of individuals, it presents a trifurcation into left anterior descending artery (LAD), left circumflex artery (LCx) and ramus intermedium (RI).

Left anterior descending artery

Responsible for supplying the interventricular septum. If the first septal or diagonal branch originates early (within 10–15 mm), the LAD is subdivided into three segments.

- **5: Left main coronary artery (LM)**

Originates from the left aortic sinus and terminates in a bifurcation (or trifurcation) into LAD and LCX (and occasionally RI). It passes between the pulmonary trunk and left atrium.

- **6: Proximal LAD (pLAD)**

Extends from the LM bifurcation to the origin of the first diagonal branch (D1). If D1 arises very proximally, pLAD may instead extend until the first major curvature change. Shown in A.5.

- **7: Medial LAD (mLAD)**

From the end of pLAD to the origin of the second diagonal branch (D2), or to the next pronounced curvature. Approximately halfway to the apex. Shown in A.5.

- **8: Distal LAD (dLAD)**

From the end of mLAD to the terminal point of the LAD, usually reaching the apex. Shown in A.5.

- **9: First diagonal branch (D1)**

First bifurcation from the LAD, extending toward the anterior surface of the left ventricle. It may arise from either pLAD or mLAD. Shown in A.6.

- **10: Second diagonal branch (D2)**

A more distal branch of the LAD, with a similar trajectory to D1. Shown in A.6.

- **17: Ramus intermedius (RI)**

An anatomical variant found in approximately 30% of the population, resulting from LCA trifurcation. It arises between the LAD and LCX and projects toward the anterolateral wall of the left ventricle. If no trifurcation is present, this branch is instead classified as D1 or first obtuse marginal branch (OM1). Shown in A.7.

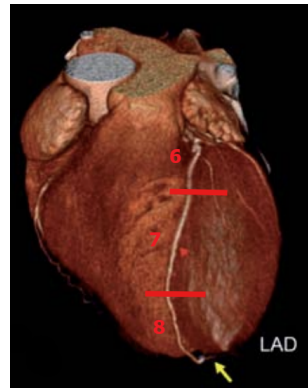


Figure A.5: Example illustrating the division of the three segments of the LAD: 6 (pLAD), 7 (mLAD), and 8 (dLAD), based on changes in vessel curvature, highlighted in red. Adapted from Pons-Lladó and Leta-Petracca (2006) [45].



Figure A.6: Illustration of LAD diagonal branches. From Pons-Lladó and Leta-Petracca (2006) [45].

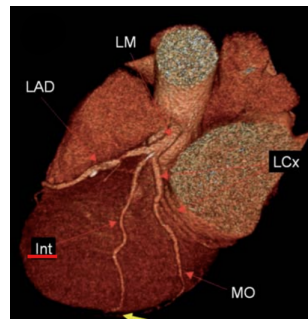


Figure A.7: Ramus intermedius (RI) highlighted in red. Adapted from Pons-Lladó and Leta-Petracca (2006) [45].

Left circumflex artery

- **11: Proximal LCX (pLCX)**

Extends from the LM bifurcation to the origin of the first obtuse marginal branch (OM1).

- **12: First obtuse marginal branch (OM1)**

Arises from the pLCx and travels perpendicularly toward the lateral wall of the left ventricle. Shown in A.8.

- **13: Distal LCX (dLCX)**

From the origin of OM1 to the end of the LCX, potentially giving rise to the left posterior descending artery (L-PDA) or left posterolateral branch (L-PLB).

- **14: Second obtuse marginal branch (OM2)**

Originates from the distal LCx. Similar to OM1 but directed more distally along the lateral wall. Shown in A.8.

- **15: Left posterior descending artery (L-PDA)**

Found in left-dominant circulations. Descends vertically in the posterior interventricular sulcus toward the apex. Shown in A.9. On the other hand, A.10 shows examples of two codominant cases.

- **18: Left posterolateral branch (L-PLB)**

Terminal branch of the distal LCx. Most commonly arises from the RCA in right-dominant cases but may also originate from the LCx.

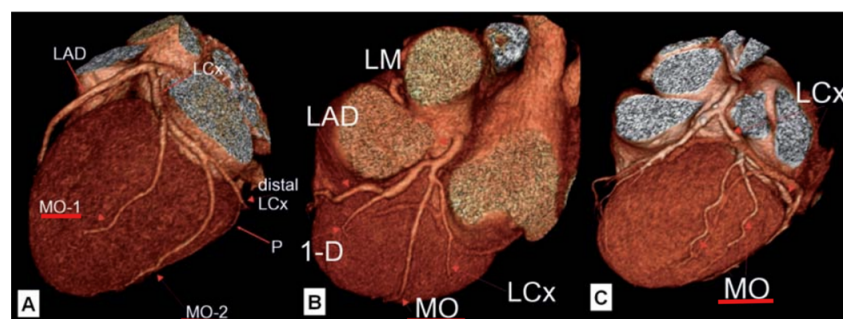


Figure A.8: Anatomy of marginal obtuse (MO) branches. A: Two MO branches are seen (1 and 2) and, also, a posterior branch irrigating the posterior aspect of the left ventricle; B: Occasionally, only a single MO branch is present which arises early from the left circumflex (LCx) and is frequently larger than the LCx itself; C: Bifurcated MO branch; LAD: left anterior descending; LM: left main; 1D: first diagonal. Adapted from Pons-Lladó and Leta-Petracca (2006) [45].

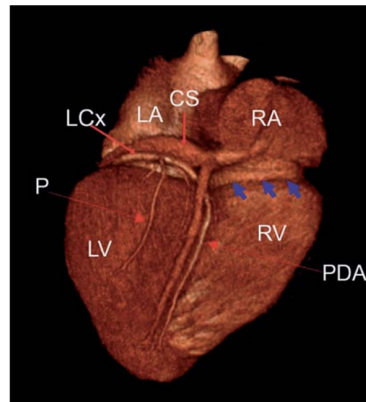


Figure A.9: Example of the anatomical dominance of the left coronary system, with a posterior descending artery (PDA) depending from the left circumflex (LCx); a posterior (P) branch of the LCx is seen irrigating the posterior aspect of the left ventricle (LV), while the right coronary artery does not reach the inferior aspect of the heart (blue arrows). CS: coronary sinus, RA: right atrium, LA: left atrium, RV: right ventricle, LV: left ventricle. From Pons-Lladó and Leta-Petracca (2006) [45].

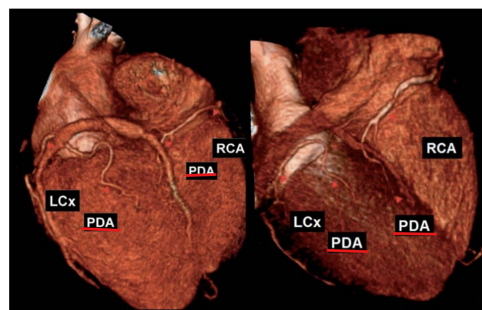


Figure A.10: Two different subjects with a balanced coronary circulation pattern: both the RCA and LCx give origin to a posterior descending artery (PDA) from their own. Adapted from Pons-Lladó and Leta-Petracca (2006) [45].

Appendix B

EXAMPLE OF MOTION ARTIFACT

The ASOCA dataset, being one of the few publicly available resources for coronary artery segmentation, presents several limitations that hinder the development of high-quality ground truth annotations. Among these, motion artifacts are particularly frequent, often caused by cardiac or respiratory movement during image acquisition. These artifacts introduce blurring, discontinuities, and deformation in the vessel structures, which significantly compromise the anatomical fidelity of the segmentations. Figure B.1 shows an example of a case from the ASOCA dataset affected by a motion artifact and incomplete segmentation.

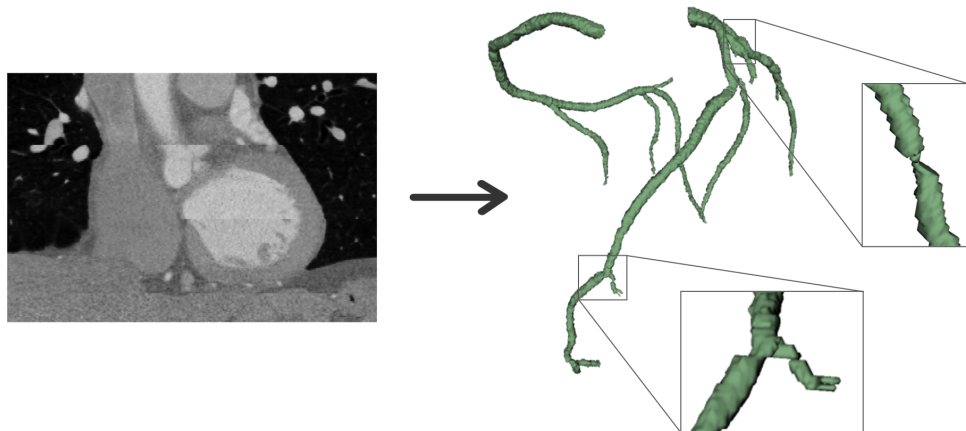


Figure B.1: Example of the case Diseased 7 from the ASOCA dataset exhibiting a motion artifact and undersegmented coronary arteries. Left: CCTA sagittal view with visible misalignment due to cardiac motion. Right: Coronary artery segmentation showing defects caused by this artifact.

Appendix C

GRAPH-BASED FEATURES

The machine learning (ML) classifiers that incorporated graph information relied on a set of handcrafted features extracted from the minimum spanning tree (MST) representation of the coronary artery centerlines. These features capture both spatial and topological characteristics of each point within the arterial tree, enabling the models to learn patterns associated with anatomical segment classification. The table below provides a detailed description of each feature used.

Table C.1: Graph-derived features used for ML coronary segment classification

Feature	Description
(Px, Py, Pz)	Spatial coordinates of each centreline point.
Node index	Unique identifier of the node in the MST traversal.
Euclidean distance to root	3D Euclidean distance from the node to the root node.
Topological depth	Number of edges between the node and the root node in the graph.
Number of neighbors	Degree of the node (number of connected neighbors) in the MST.
Geodesic distance	Sum of edge lengths along the shortest path from the node to the root node.
DFS visit order	Order in which the node is visited in a depth-first search traversal.

Appendix D

DEEP LEARNING MODELS TRAINING CURVES

D.1 GraphSAGE training curves

The loss and accuracy trends over 600 training epochs of the GraphSAGE model, applied within the GNN-based coronary segment labeling strategy, are presented in Figures D.1 and D.2 for the right coronary artery (RCA), and in Figures D.3 and D.4 for the left coronary artery (LCA).

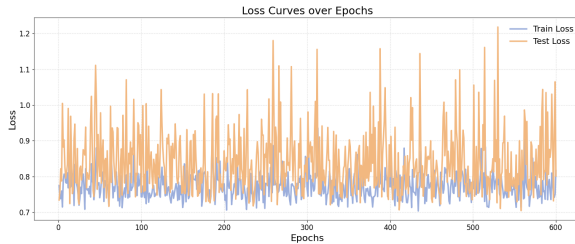


Figure D.1: Loss curves over epochs for the RCA GraphSAGE model.

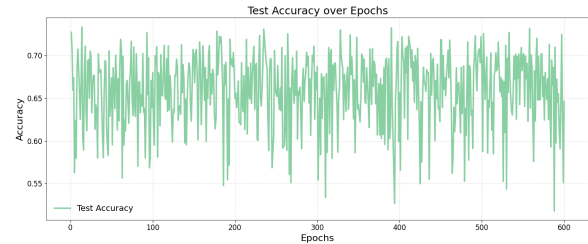


Figure D.2: Testing accuracy over epochs for the RCA GraphSAGE model.

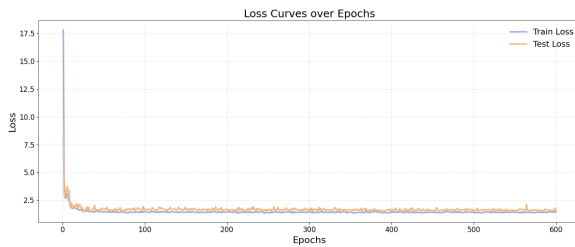


Figure D.3: Loss curves over epochs for the LCA GraphSAGE model.

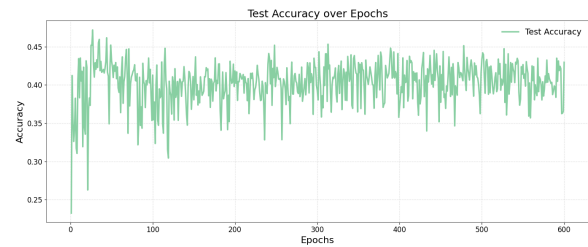


Figure D.4: Testing accuracy over epochs for the LCA GraphSAGE model.

D.2 nnU-Net training curves

Figure D.5 presents the training dynamics of the nnU-Net model over 2000 epochs, corresponding to the direct multi-class segmentation task of the 19 coronary artery segments.

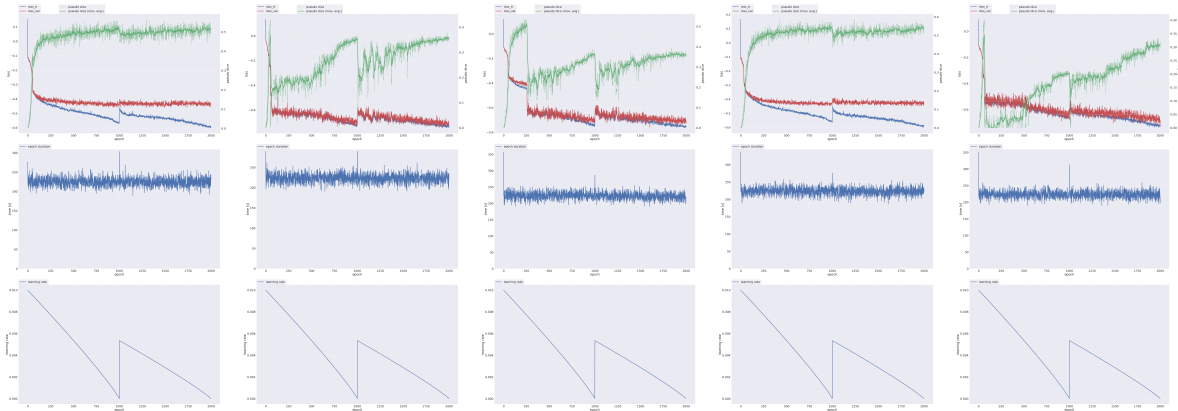


Figure D.5: Training curves of the nnU-Net model for each of the five cross-validation folds over 2000 epochs. The top plot displays the training loss, validation loss, and pseudo-Dice score evolution, the middle plot shows the duration of each epoch, and the bottom plot illustrates the learning rate schedule applied during training.

Appendix E

SOURCE CODE ACCESS

The complete implementation of the methods and experiments presented in this thesis is available at the following repository:

<https://github.com/maren00/Automatic-Labeling-of-Coronary-Artery-Segments-Multi-Strategy-Development-and-Evaluation.git>